An Empirical Statistical Model Relating Winds and Ocean Surface Currents: Implications for Short-term Current Forecasts

by
Brian Christopher Zelenke

A THESIS

submitted to

Oregon State University

in partial fulfillment of
the requirements for the
degree of

Master of Science

Presented December 2, 2005
Commencement June 2006

AN ABSTRACT OF THE THESIS OF

Brian Christopher Zelenke for the degree of Master of Science in Oceanography presented on December 2, 2005.

Title: An Empirical Statistical Model Relating Winds and Ocean Surface Currents: Implications for Short-term Current Forecasts

Abstract approved:

P. Michael Kosro

An empirical statistical model is developed that relates the non-tidal motion of the ocean surface currents off the Oregon coast to forecasts of the coastal winds. The empirical statistical model is then used to produce predictions of the surface currents that are evaluated for their agreement with measured currents. Measurements of the ocean surface currents were made at 6 km resolution using Long-Range CODAR SeaSonde high-frequency (HF) surface current mappers and wind forecasts were provided at 12 km resolution by the North American Mesoscale (NAM) model. First, the response of the surface currents to wind-forcing measured by five coastal National Data Buoy Center (NDBC) stations was evaluated using empirical orthogonal function

(EOF) analysis. A significant correlation of approximately 0.8 was found between the majority of the variability in the seasonal anomalies of the low-pass filtered surface currents and the seasonal anomalies of the low-pass filtered wind stress measurements. The U and the V components of the measured surface currents were both shown to be forced by the τ^y and τ^x components of the wind-stress at the NDBC stations. Next, the NAM wind forecasts were tested for agreement with the measurements of the wind at the NDBC stations. Significant correlations of around 0.8 for τ^y and 0.6 for τ^x were found between the seasonal anomalies of the low-pass filtered wind stress measured by the NDBC stations and the seasonal anomalies of the low-pass filtered wind stress forecast by the NAM model. Given the amount of the variance in the winds captured by the NAM model and the response of the ocean surface currents to both components of the wind, bilinear regressions were formed relating the seasonal anomalies of the low-pass filtered NAM forecasts to the seasonal anomalies of the low-pass filtered surface currents. The regressions turned NAM wind forecasts into predictions of the seasonal anomalies of the low-pass filtered surface currents. Calculations of the seasonal cycle in the surface currents, added to these predicted seasonal anomalies, produced a non-tidal estimation of the surface currents that allowed a residual difference to be calculated from recent surface current measurements. The sum of the seasonal anomalies, the seasonal cycle, and the residual formed a prediction of the non-tidal surface currents. The average error in this prediction of the surface currents off the Oregon coast remained less than 4 cm s^{-1} out through 48 hours into the future.

ACKNOWLEDGEMENTS

Oregon State University's Coastal Ocean Mapping Lab (P.M. Kosro, W. Waldorf, and Anne Dorkins) for installation and operation of the HF equipment. Phil Barbour, Dudley Chelton, Priscilla Newberger, and Roger Samelson for providing access to and understanding of the NAM model data. Jack Barth for access to additional data sets and suggestions for future work. Yvette Spitz for providing use of computer resources to assist in data processing. Nancy Kerkvliet, Kipp Shearman, and Ted Strub for their guidance and service as my committee. Roberto Venegas for the enlightening discussions and friendship. Mike Kosro for serving as my advisor here at COAS… and all the support, guidance, and patience that entailed. Most of all thanks to my wife Carol Zelenke and my son Ethan Zelenke for the motivation and love.

This work was supported in part by the National Science Foundation as part of the GLOBEC program, under grant OCE-0000734, and by the National Aeronautics and Space Administration Space Grant Program, under grant NGT5-40103. This is contribution number 268 of the U.S. GLOBEC Program.

TABLE OF CONTENTS

Page

TABLE OF CONTENTS (Continued)

Page

LIST OF FIGURES

LIST OF FIGURES (Continued)

LIST OF FIGURES (Continued)

LIST OF TABLES

LIST OF APPENDIX TABLES

An Empirical Statistical Model Relating Winds and Ocean Surface Currents: Implications for Short-term Current Forecasts

1 Introduction

Forecasts of the winds off the coast of Oregon are made routinely that show both magnitude and direction of the wind speed at 12 km mesoscale resolution. No such forecasts of the ocean currents off Oregon are presently made on a regular basis. Hourly measurements, however, are being made of the surface currents off Oregon at 6 km resolution using a coastal network of high-frequency radio (HFR) systems. This paper derives and evaluates an empirical statistical model relating these surface current measurements and wind forecasts.

The currents off Oregon have a strong seasonal cycle with distinct spring/summer and fall/winter conditions (Huyer et al., 1979; Strub et al., 1987a). In the spring, a southward shift in the winds occurs around the month of April causing a "spring transition" in the currents. Throughout the spring and summer these southward winds induce an offshore Ekman transport. This offshore flow results in a drop in sea level and the upwelling of cooler, denser water from below (Allen, 1973; Huyer et al., 1975; Jones and Halpern, 1981). The decrease in density from the coast out to sea induces the observed southward geostrophic flow down the Oregon coast in the form of a surface intensified coastal jet (Huyer et al., 1979). The trend is the opposite in the fall and winter. Around the month of October the winds shift from southward to northward. These northward winds carry warmer, less dense surface waters shoreward and a downwelling circulation results. Throughout the year the wind-forcing is subject to changes in intensity and reversals in direction, allowing for sporadic periods of upwelling and downwelling out of season.

1.1 Surface Current Measurements

Measurements of the surface currents were made by the Oregon State University Ocean Currents Mapping Lab, as part of the United States GLOBEC (GLOBal ocean ECosystems dynamics) Northeast Pacific Program, using Long-Range SeaSonde® HFR systems manufactured by CODAR[1] Ocean Sensors, Ltd. These surface current mappers were located along the coast of Oregon and northern California (Table 1; Figure 1).

---

[1] CODAR was originally an acronym coined by Dr. Donald Barrick, President of CODAR Ocean Sensors, which stood for "Coastal Ocean Dynamics Applications Radar" (Donald Barrick, *personal communication*, November 1, 2005). CODAR has since evolved into a word in and of itself in the HFR community and, as such, is no longer considered an acronym.

Table 1. Locations of the HFR sites used to measure the surface currents and of the National Data Buoy Center (NDBC) stations that measured the winds. NDBC stations with number designators were 3-meter discus buoys. Those NDBC stations with letter designations were land-based Coastal-Marine Automated Network (C-MAN) stations.

Name	Latitude	Longitude
HFR		
Yaquina Head (YHL1)	44° 40' 34" N	124° 4' 38" W
Winchester Bay (WIN1)	43° 39' 57" N	124° 12' 23" W
Cape Blanco State Park (CBL1)	42° 50' 12" N	124° 33' 56" W
Point Saint George (PSG1)	41° 47' 4" N	124° 15' 17" W
NDBC		
46050	44° 37' 16" N	124° 31' 42" W
NWPO3	44° 36' 48" N	124° 4' 00" W
CARO3	43° 20' 30" N	124° 22' 30" W
46027	41° 51' 6" N	124° 22' 54" W
46022	40° 46' 53" N	124° 32' 31" W

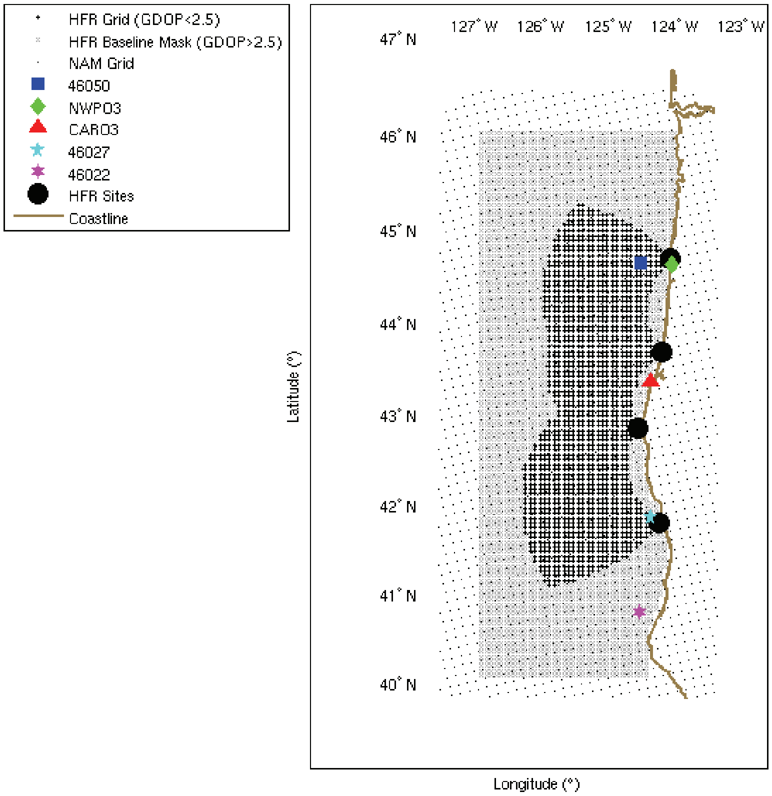

Figure 1. Map of the locations of the 12 km resolution North American Mesoscale (NAM; formerly Eta) model gridpoints, 6 km resolution HFR gridpoints, the HFR station locations, and the NDBC station locations. The area of the HFR grid shaded gray is the area masked-out by the GDOP baseline mask.

HFR systems measure the speed, distance, and direction of the surface currents (Barrick et al., 1977; Lipa and Barrick, 1983). Surface currents are measured by HFR using the principle of Bragg scattering with an uncertainty on the order of 7 cm s^{-1} (Chapman and Graber, 1997). The conducting medium of seawater permits transmission of an electromagnetic (EM) ground wave along the surface of the water. The ground wave propagates beyond the line-of-sight allowing measurements up to 200 km from shore. The transmitted EM wave is scattered by all waves on the ocean's surface with enhanced backscatter occurring near the Bragg wavelength, which is one-half that of the EM wave (Figure 2).

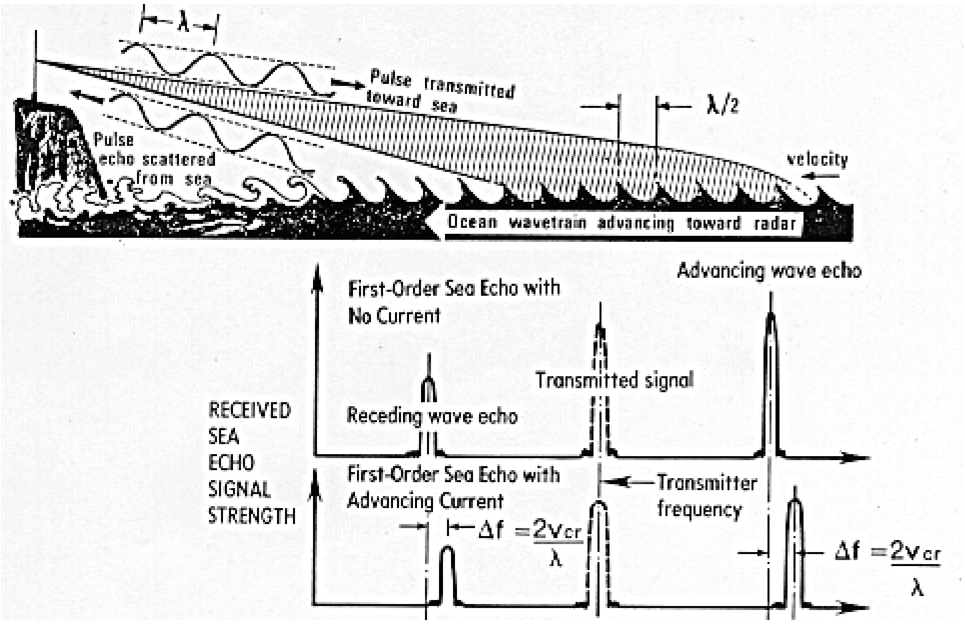

Figure 2. "Sketch showing the principles of first-order HF Bragg scatter from the sea, and resulting signal echo spectra without and with an underlying current" (from Barrick et al., 1977).

The HFR sites transmitted at frequencies around 5 MHz, corresponding to a wavelength, λ, of 60 m thus giving enhanced scattering off of 30 m, $\left(\frac{\lambda}{2}\right)$, ocean waves. Radial currents, those moving either toward or away from the sites, are mapped using the spectral peaks generated because of the enhanced scattering at the Bragg wavelength (i.e., the first-order Bragg sea-echo). The echo from the scattered EM waves experiences a Doppler shift in frequency due to the total velocity of the wave, which is the phase speed of the reflecting ocean wave plus the underlying current. The phase speed of the reflecting wave is known from the deep-water dispersion relation, $\pm\sqrt{\frac{g\lambda}{4\pi}}$ where g is the acceleration of gravity and the sign indicates whether the wave is moving towards (+) or away (-) from the HFR site. If there were no underlying current, the Bragg scatter would experience a Doppler shift due only to the phase speed of the reflecting wave. However, an underlying current moving towards or away from the HFR site causes a shift in frequency, Δf, in addition to the Doppler shift, equal to $\frac{2v_{cr}}{\lambda}$, where v_{cr} is the radial speed of the surface current. It is this additional shift in the received sea echo that indicates the speed of the current and whether the current is moving towards or away from the HFR site.

Offshore distance is determined by range-gating the transmitted signal. The time delay of the scattered signal after transmission is multiplied by the speed of the EM wave (i.e., the speed of light) to determine the distance of the scattering wave. The

SeaSonde sweeps its transmitted frequency over about 50 kHz so that return reflections do not interfere with the transmitted signal.

The direction of each current measurement is determined from the geometry of the receive antenna patterns. The receive antenna is formed from a series of three co-located antennas, one monopole and two loops crossed to have their axes of maximum response at right angles. The differing voltages induced by the returning EM wave in the two cross loops and the center monopole are compared using CODAR Ocean Sensor's version of the MUSIC algorithm (Schmidt, 1986) to get the bearing to the target waves (Barrick and Lipa, 1997; Barrick and Lipa, 1999).

Bragg reflections are received from numerous waves over a range of distance and from a wide range of directions. The calculated radial velocity values from these reflections are averaged into range and azimuth bins to form a map. Since single HFR sites can only measure radial currents, a minimum of two sites with overlapping measurements is required to calculate vector surface currents. The accuracy of the total vector surface currents is dependent on the geometry of the intersecting radial velocities. This geometric dependence is characterized as the geometric dilution of precision (GDOP) (Barrick, 2002).

1.2 Model Formation

In the following analysis, we will use these measurements and the predicted winds to derive and evaluate an empirical short-term surface current prediction system. In Chapter 2 the surface current measurements are evaluated for their relationship to the wind stress as measured by the NDBC stations. Empirical orthogonal function (EOF) analysis was used to understand the major modes of variability observed in the surface current measurements and the NDBC measurements of wind stress. A distinct correlation was found between the first and second EOFs of the surface currents and NDBC measurements, indicating that the majority of the variability in the surface currents correlated well with the measured winds.

Chapter 3 develops an empirical statistical model to predict the response of the surface currents to coastal winds forecast by the National Centers for Environmental Prediction (NCEP) NAM model. The NAM model was found by Perlin et al. (2004) to be better correlated with National Aeronautics and Space Administration (NASA) Quick Scatterometer (QuikSCAT) winds off the Oregon and northern California coasts than either of two nested regional models, the Coupled Ocean–Atmosphere Mesoscale Prediction System (COAMPS) of the Naval Research Laboratory or the Advanced Regional Prediction System (ARPS) of the University of Oklahoma. In Section 3.3 of this thesis, the measurements at the NDBC stations are compared with the NAM forecasts over a two year period and reasonable agreement is found at time-scales greater than five days and shorter than seasonal. The understanding gained from this comparison suggests the NAM model will be suitable on which to base a forecast current model.

Descriptions of the NAM model physics and its architecture are given in Black (1994), Janjić (1994), and Rogers (2001). Forecasts of the 10 m surface wind fields were obtained from the portion of the 12 km NAM model grid shown in Figure 1. The NAM model issued forecasts at three hour intervals out to 48 hours into the future each day at 0000 UTC (for your reference: at 0-h, 3-h, 6-h, 9-h, 12-h, 15-h, 18-h, 21-h, 24-h, 27-h, 30-h, 33-h, 36-h, 39-h, 42-h, 45-h, and 48-h) over all the times considered in this analysis. This allowed the surface currents to likewise be predicted two days into the future at those same forecast hours.

In Section 3.4, a model is derived from bilinear regression between the seasonal anomalies of the low-pass filtered U and V time-series of surface currents mapped to the HFR gridpoints and NAM forecasts of the winds interpolated to those gridpoints. The model adds the seasonal cycle to the predicted seasonal anomalies to produce low-pass filtered surface currents. Recent hourly surface current measurements were used to ground-truth the low-pass filtered predictions to those most recent measurements of the surface currents, producing a residual whose addition completed the model. The model was tested over 117 days between March 2, 2005 and July 10, 2005. Correlations between the predictions and the measurements in the region between 42°-44° N around 125° W were in excess of 0.7 in both the V and U components out to 48 hours into the future.

2 Comparison of NDBC Station Wind Measurements to Surface Currents

This chapter examines the link between the surface currents and the coastal winds off of Oregon using EOFs. The understanding of the wind-forced circulation gained in the following analysis demonstrated the need for localized predictions of both the north-south and east-west components of the winds to accurately predict the wind-forced surface current response.

2.1 Data Processing

Archived data were available from four Long-Range CODAR SeaSonde HFR systems beginning in August of 2002. Starting from north to south, the first three sites were located in the State of Oregon at Yaquina Head (YHL1), Winchester Bay (WIN1), and Cape Blanco State Park (CBL1), with the southernmost site located in California at Point Saint George (PSG1) (Figure 1; Table 1). Each HFR site produced hourly maps of radial surface currents on a 5° azimuthal grid with 5.85 km spacing (Figure 3).

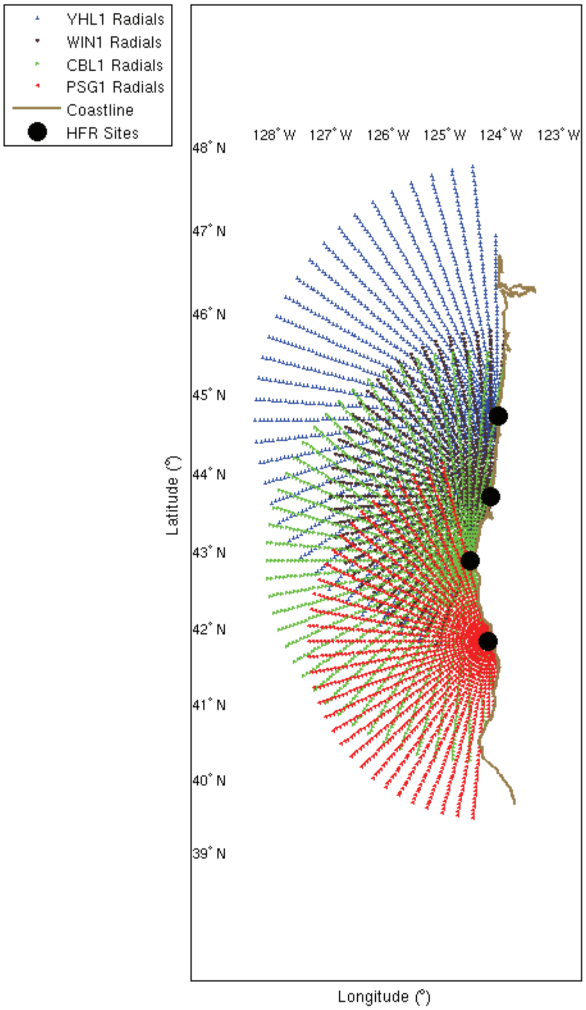

Figure 3. Map of the extent of the radial coverage from the four HFR sites. Note the areas of overlap between the four sites, where total current vectors could be produced.

In order to ensure a balanced representation of the seasonality in the time series, a two-year time period was chosen with an equal number of seasons. With the months of September through November defined as fall, December through February as winter, March through May as spring, and June through August as summer, a time period of two years from September 2002 through August 2004 was selected for analysis.

The radial velocities from each of the four HFR sites were screened for anomalous measurements (Appendix A). This data checking was done so that a spurious radial velocity would not get averaged into the calculation of a surface current vector. This screening resulted in an approximately 2% data reduction and completely eliminated data placed over land due to direction-finding errors. These screened radial velocity measurements were then combined into total current vectors using version 4.1 of the HFRadarmap toolbox for MATLAB (Cook & Paduan, 2001; Cook 2004). The processing by the HFRadarmap toolbox resulted in an hourly time series of the U and V components of the surface currents in cm s^{-1} at each point in the HFR grid. Missing measurements in the time series at each grid point were flagged.

The time series of wind speed were downloaded from the National Data Buoy Center (NDBC) website from five stations adjacent to or within the HFR coverage area (46050, NWPO3, CARO3, 46027, and 46022) over the same two year time period as for the HFR data (Figure 1; Table 1; NDBC, 2005). The hourly time-series of wind speeds and directions were then resolved into their V and U components. Missing measurements in the time series at each station were filled in by regression with the measurements from the other stations (Figures 4 & 5).

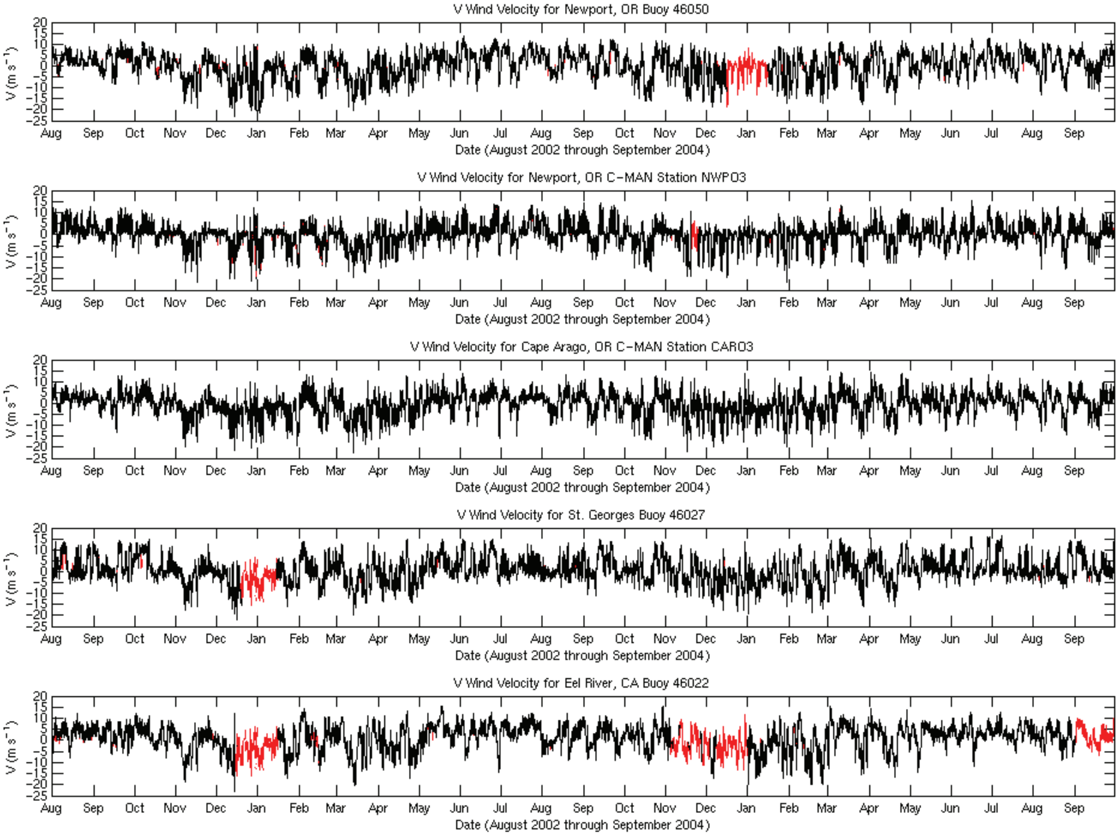

Figure 4. Time-series of the V (north-south) component of wind velocity measured over the two years at the NDBC stations. The black lines represent real measurements while the red lines represent those portions of the time series that were interpolated. The percentages of each of the time-series that were interpolated are as follows: 46050 (4.2%), NWPO3 (1.6%), CARO3 (0%), 46027 (3.3%), 46022 (14.4%).

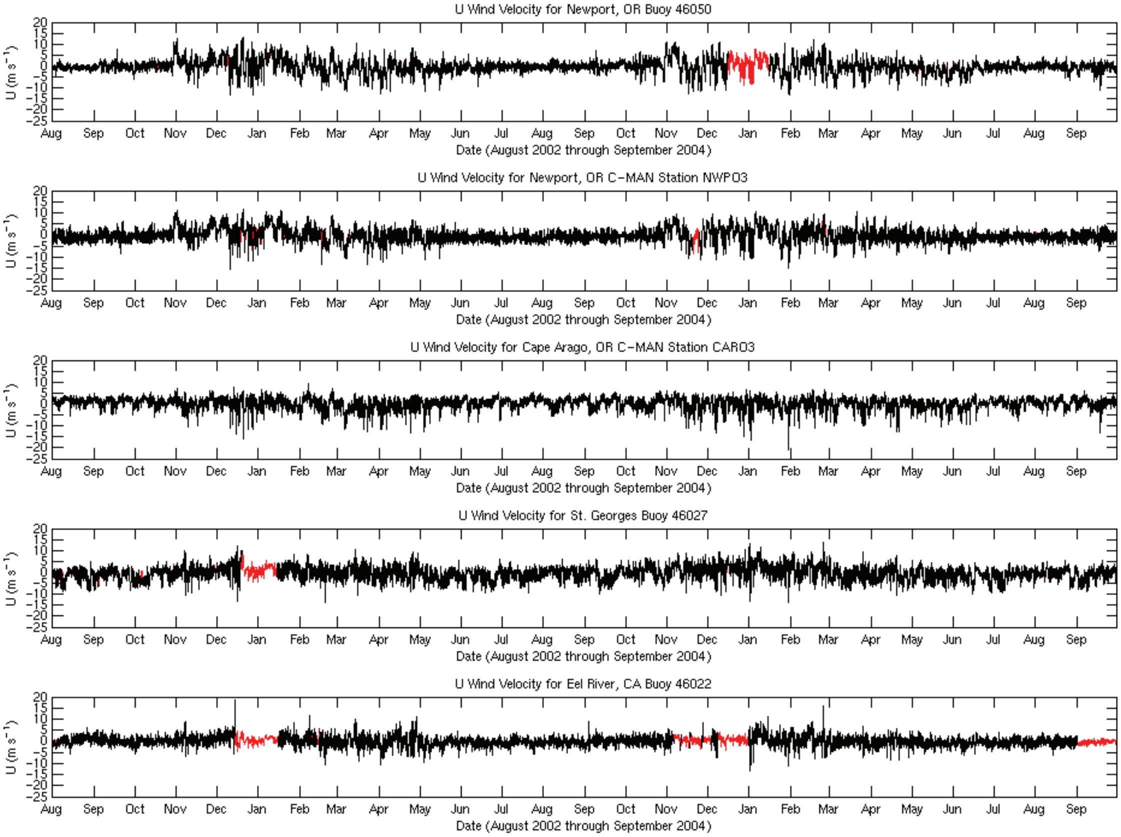

Figure 5. As in Figure 4, for the U (east-west) component of wind velocity.

This gap-filling of the time series at each station was accomplished first by a linear regression with the measurements made by the closest station. Then, to fill in any remaining gaps, a multiple linear regression was made using the measurements at the other three stations. The continuous time series were then converted from hourly U and V 10 m wind speeds into τ^x and τ^y, components of wind stress in N m^{-2} using the drag coefficients of Large and Pond (1981), modified by Trenberth et al. (1990) for low wind speeds.

The hourly time series of surface currents at each HFR gridpoint and the wind stress measurements at the NDBC stations were then low-pass filtered using the OSU Cosine-Lanczos filter, a 60+1+60 point filter with a half-amplitude point at 40 hours, a half-power point at 46.6 hours, and the following generating function for the filter weights:

$$\frac{1}{2}\cdot\left[1+\cos\left(\frac{\pi t}{61}\right)\right]\cdot \mathrm{sinc}\left(\frac{2t}{40}\right)$$

The OSU filter removed the diurnal and semidiurnal tides, inertial energy, and all higher frequencies (Beardsley et al., 1985). The seasonal cycle in the low-pass filtered data was then calculated for the time series at each HFR gridpoint and NDBC station through a fit to the annual and semi-annual harmonics in each U and V parameter:

$$S_t = S_0 + S_a \cdot \cos(\omega t + \varphi_a) + S_s \cdot \cos(2\,\omega t + \varphi_s)$$

where S_t = Time-series, S_0 = Long term mean, S_a = Annual amplitude, S_s = Semiannual amplitude, ω = Annual radian frequency = $\frac{2\pi}{365.24\ \text{days}}$, t = Time, φ_a and φ_s = Annual and semi-annual phase (Figures 6 & 7; Strub et al., 1987b; Kosro 2003). The seasonal cycle was saved separately and then subtracted from each time series to yield seasonal anomalies of the low-pass filtered data (Figures 8 & 9; discussed in Section 2.4.1).

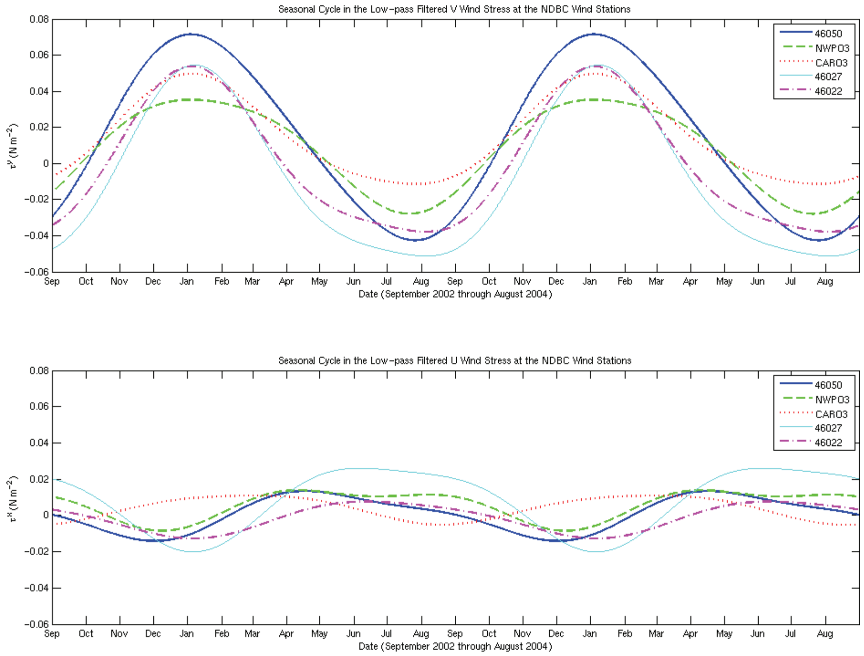

Figure 6. Fits to the north-south (top panel) and east-west (bottom panel) seasonal cycle of winds at the NDBC stations.

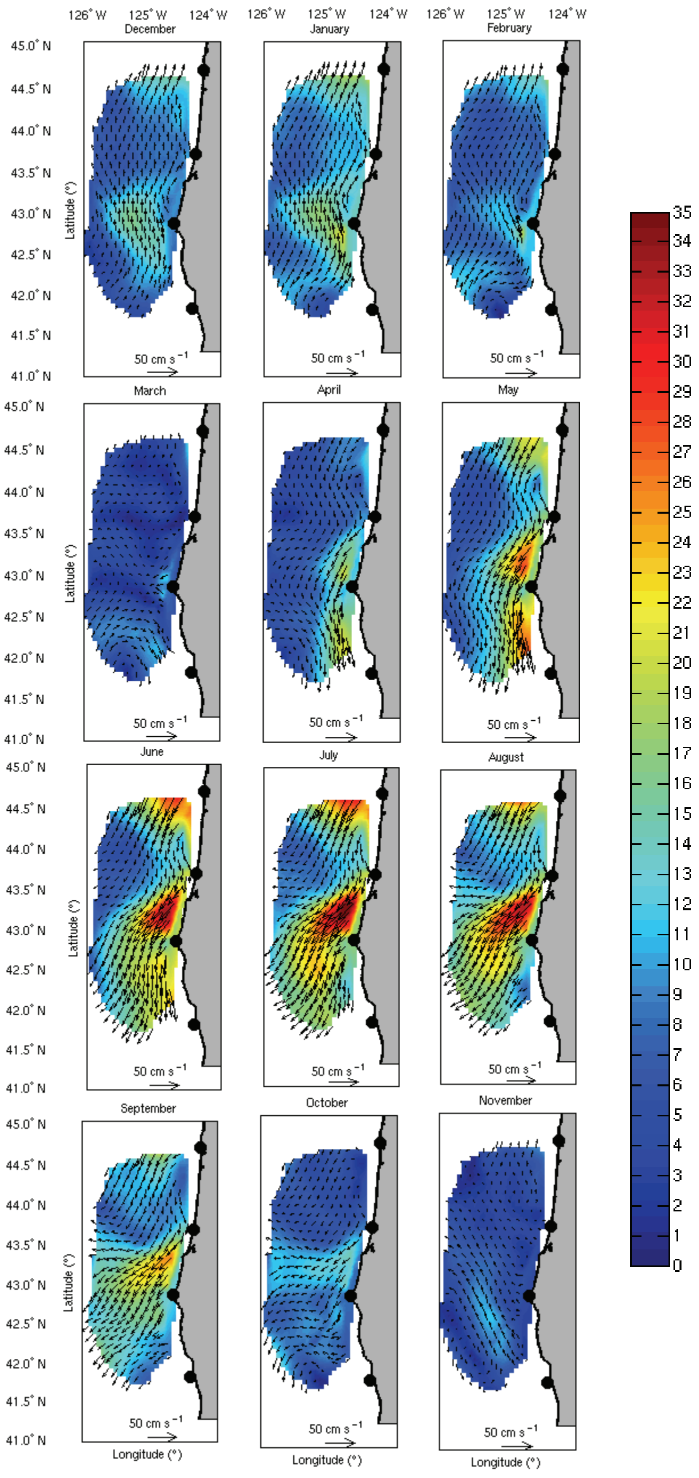

Figure 7. Fit to the seasonal cycle in the surface currents at the first of each month. Color shading is velocity in cm s^{-1}. Black dots along the coast are HFR sites. Surface current vectors are plotted at one-fourth density.

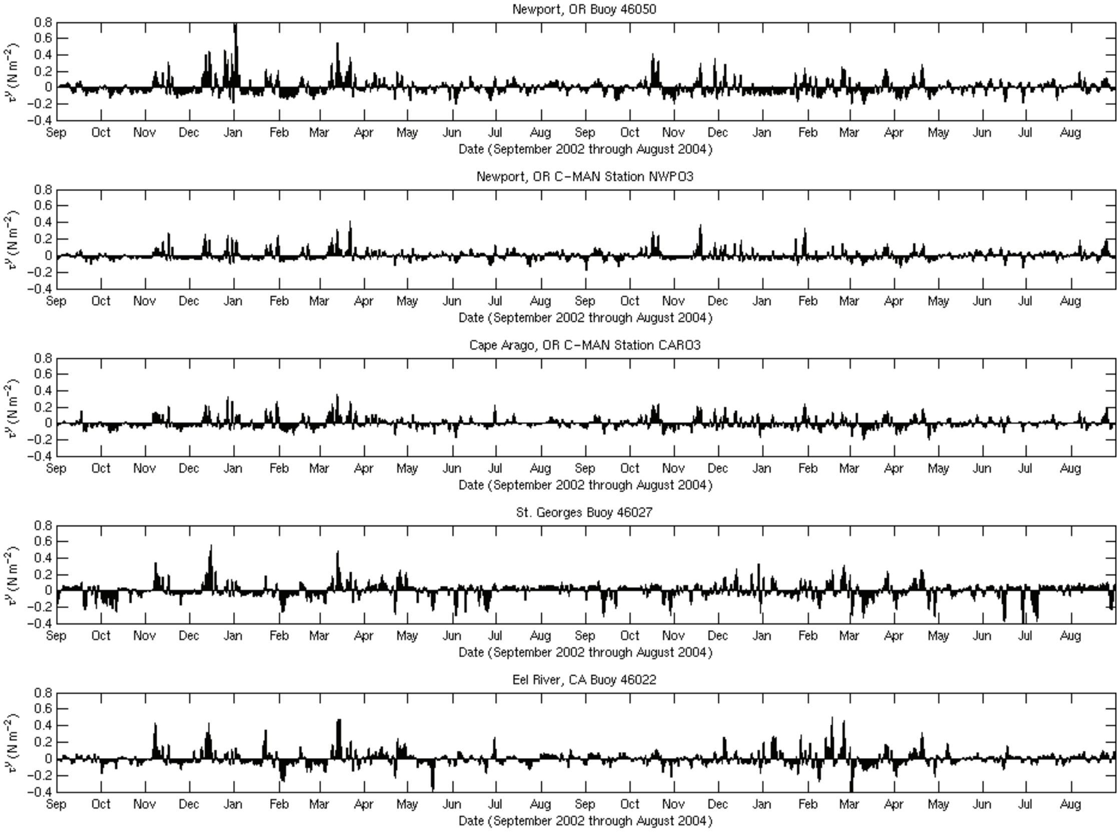

Figure 8. Seasonal anomalies of the low-pass filtered north-south component of the wind stress at the NDBC stations. Seasonal anomalies of the low-pass filtered V surface currents were also made from the time-series at each HFR gridpoint (not plotted).

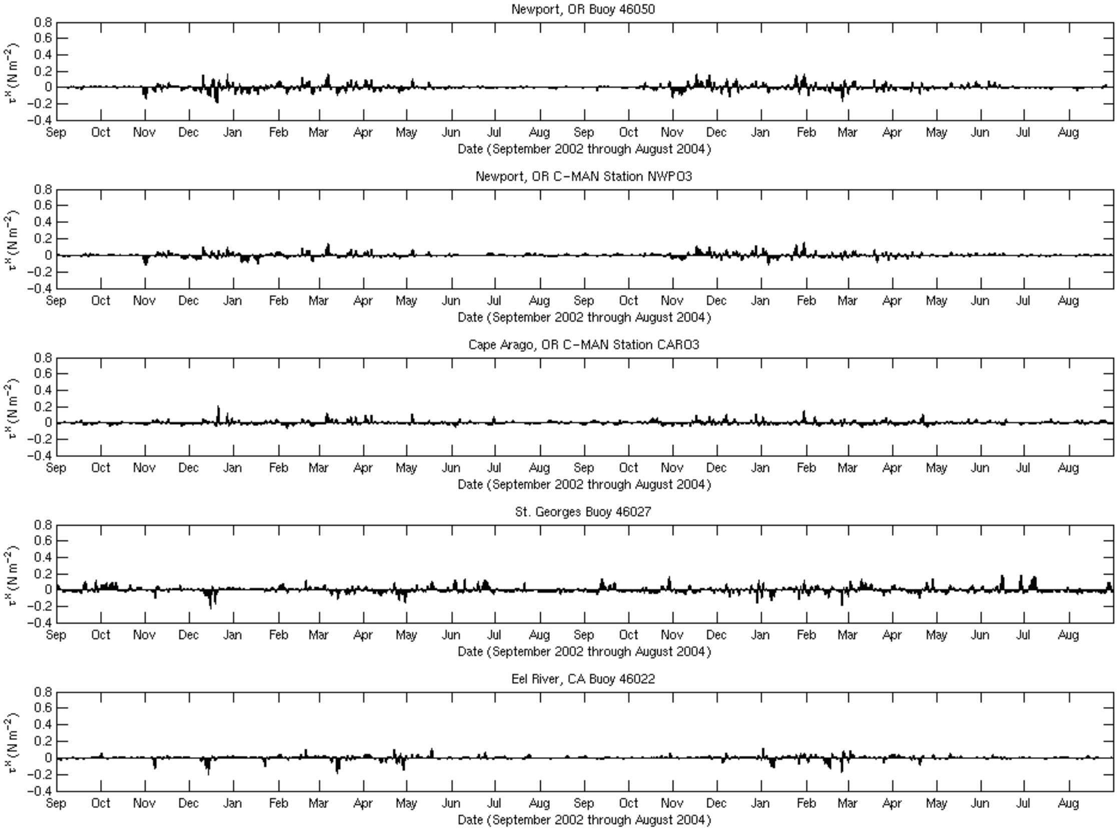

Figure 9. As in Figure 8, except for the low-pass filtered U component of the wind stress at the NDBC stations.

Accuracy of total surface current vectors formed through the combination of measured HFR radial velocities depends on grid geometry, with the error of the total current vectors increasing as the radials used in their computation become more nearly collinear (Figure 3; Barrick, 2002). Regions of the HFR measurement grid where the angles between radar sites and the gridpoints were too nearly parallel were thus masked-out (Figure 1). Application of this “baseline mask” to the HFR data eliminated those gridpoints where the GDOP was above 2.5 because the angle between the radial velocities measured by the HFR systems were either too close to 0° (thus increasing uncertainty in the V component) or 180° (increasing uncertainty in the U component).

2.2 Analysis Methods

EOF analysis was used to compare the response of the seasonal anomalies of the low-pass filtered surface current measurements to the seasonal anomalies of low-pass filtered wind stress at each of the NDBC stations. Low-pass filtering the time series and extracting the seasonal cycle ensured that tidal variability and seasonality would not dominate the variance in the EOFs.

EOF analysis requires a continuous time-series at each point in the analysis (Davis, 1976). It is not a requirement of EOF analysis, however, that the points in the time-series be sampled at a constant rate (although irregular sampling does preclude later computations of cross-spectra using the resultant EOF amplitude time-series). Since only 573 of the HFR gridpoints had no missing data, out of the 1548 with measurements in the two year time series with the baseline mask applied, a number of hours were omitted from the surface current time-series to expand the coverage area. Gathering only those hours in the surface current time series with at least 1350 measurements produced a field of 935 gridpoints where data were always present and preserved sampling during winter 2003/2004 (Figures 10 & 11a). This eliminated 2105 hours out of 17544 (12%) from further analysis. These same hours were dropped from the wind analysis for consistency.

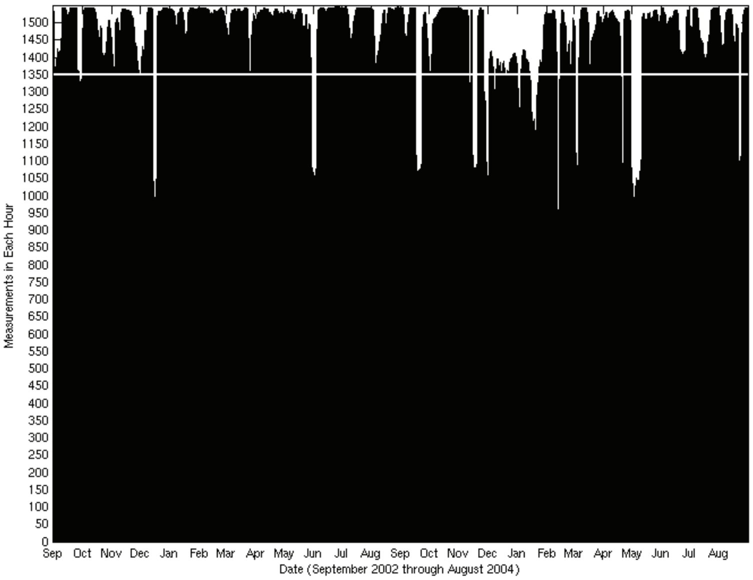

Figure 10. Number of total current vectors formed each hour from the HFR measurements over the two years from September 2002 through August 2004. White line at 1350 measurements per hour was selected as the minimum number of measurements required in a map of the surface currents for that map to be valid.

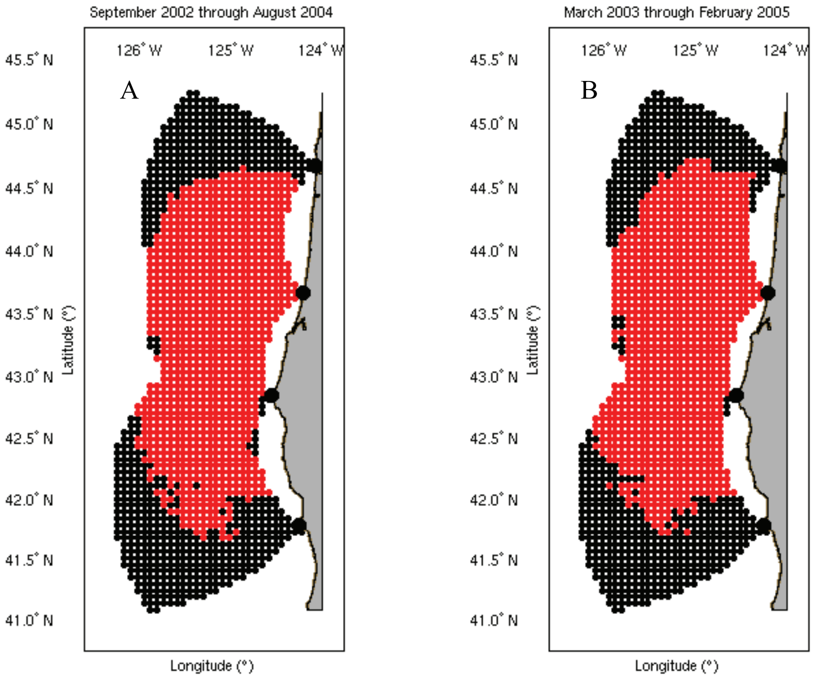

Figure 11. The portion of the HFR grid is plotted where the GDOP is less than 2.5. Gridpoints in red are locations where surface current data were always measured in those hours with at least 1350 measurements. Black points did not always have readings in those hours with the minimum 1350 point criterion applied. Panel A is for the two years from September 2002 through August 2004, during which 15439 of the 17544 (88.0%) hours satisfied the 1350 measurements per hour requirement. Panel B is the two years from March 2003 through February 2005, during which 14813 of the 17544 (84.4%) hours satisfied the 1350 measurements per hour requirement. Large black dots along the coast are HFR sites.

The U and V components of the surface current time-series were then analyzed together for vector EOFs (Davis, 1976). MATLAB's "princomp" function, which uses a singular value decomposition of the data matrix, was used to calculate the EOFs (MathWorks, 2005). Similarly, wind stress τ^x and τ^y from the five NDBC wind stations were gathered into a single data matrix and analyzed for EOFs in the same way.

2.3 Results

2.3.1 Empirical Orthogonal Functions

The results of the EOF analysis on surface currents are shown in Figures 12-14.

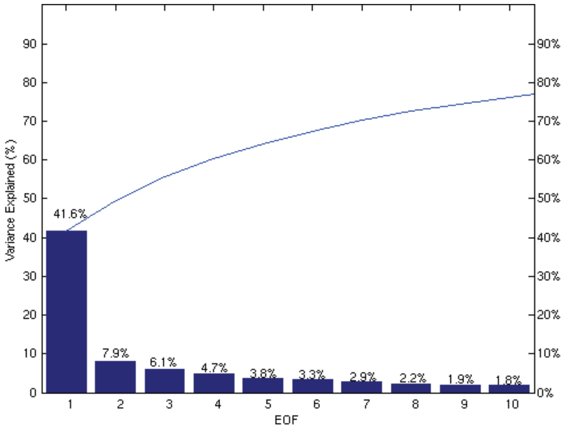

Figure 12. Percentage of the total variance in the seasonal anomalies of the low-pass filtered surface current measurements captured by each EOF mode. EOFs were calculated over the two years from September 2002 through August 2004 for the 88.0% of measurement hours that met the criterion of at least 1350 measurements per hour.

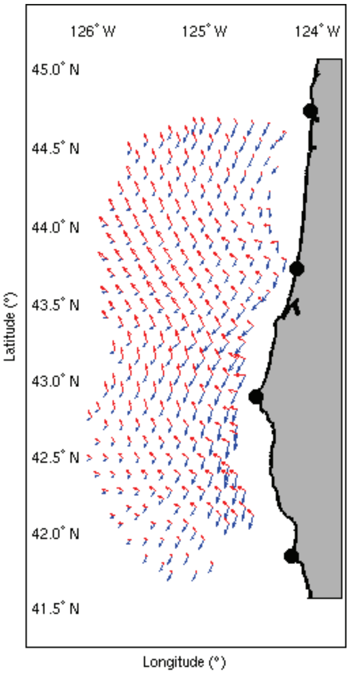

Figure 13. Shapes of the two most energetic EOF modes of the seasonal anomalies of the low-pass filtered surface current measurements. Blue is the mode shape of the first EOF; red is the mode shape of the second EOF. The magnitudes of the vectors in the EOF shapes can only be compared to one another within the same mode. The relative contribution of each EOF to the total variance is contained in the EOF amplitudes (Figure 14), rather than in the mode shapes. Black dots along the coast are HFR sites. EOF vectors are plotted at one-fourth density.

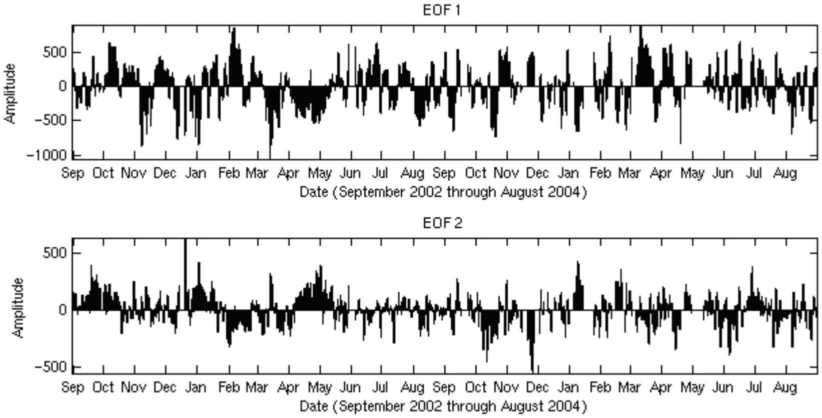

Figure 14. Time-varying amplitudes of the two most energetic EOF modes of the seasonal anomalies of the low-pass filtered HFR surface current measurements.

41.6% of the variance in the seasonal anomalies of the low-pass filtered surface currents was captured in the first EOF, with 7.9% in the second (Figure 12). Later analyses showed that EOFs three and higher were not significantly correlated with wind forcing and, therefore, are not considered (Section 2.3.2). The current fluctuations represented by the first EOF are predominantly alongshore (Figure 13). That first EOF mode has the same sign of the alongshore current throughout the map, becoming stronger and more meridional toward shore. The shape of EOF 2 is largely that of a cross-shore current and maintains the same sign of the cross-shore current. In the shape of second EOF, the currents become weaker and increasingly zonal closer to shore north of Cape Blanco but stronger and less zonal towards shore south of Cape Blanco. The time-varying amplitudes of the first two EOF modes are plotted in Figure 14. While the full time-series of EOF modes are uncorrelated with one another, there are periods within the time-series where the amplitudes co-vary (for example, in April through mid-May of 2003; Figure 14). Integral time scales of the first two EOFs were around five days (Davis, 1976 & 1977; Sciremammano, 1979).

In the EOF analysis of the seasonal anomalies of the low-pass filtered wind stress measured by the NDBC stations, 67.6% of the variance was accounted for in the first EOF, with 15.6% in the second (Figure 15). The shapes of the two most energetic EOF modes of the wind are plotted in Figure 16. The mode shapes of the first two EOFs are dominated by the north-south stress component. While τ^y in the first EOF has the same sign at all five NDBC stations, there is a sign reversal of τ^y in the second EOF at the two stations south of Cape Blanco. Thus EOF 2 can describe enhanced upwelling forcing north or south of Cape Blanco, depending on the sign of the amplitude. The time-varying amplitudes of the first two EOFs are shown in Figure 17. Decorrelation time scales were approximately 35 hours and 75 hours for EOFs 1 and 2, respectively.

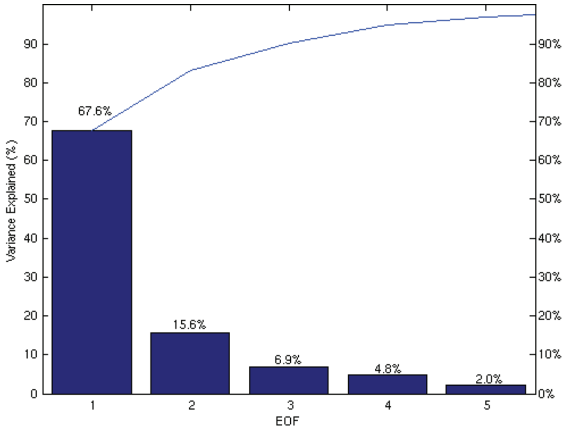

Figure 15. Percentage of the total variance in the seasonal anomalies of the low-pass filtered NDBC wind stress measurements captured by each EOF mode. EOFs were calculated over the two seasonal years from September 2002 through August 2004 for those measurements made at the same times as the measurements used in the calculation of the surface current EOFs.

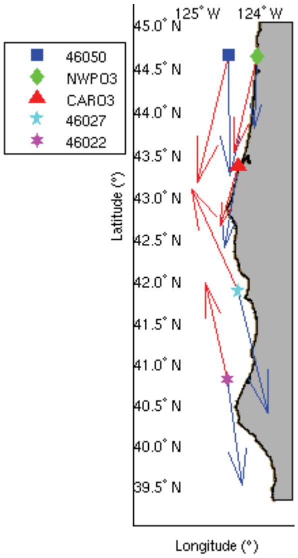

Figure 16. Shapes of the two most energetic EOF modes of the low-pass filtered NDBC wind stress measurements. Blue is the mode shape of the first EOF; red is the mode shape of the second EOF.

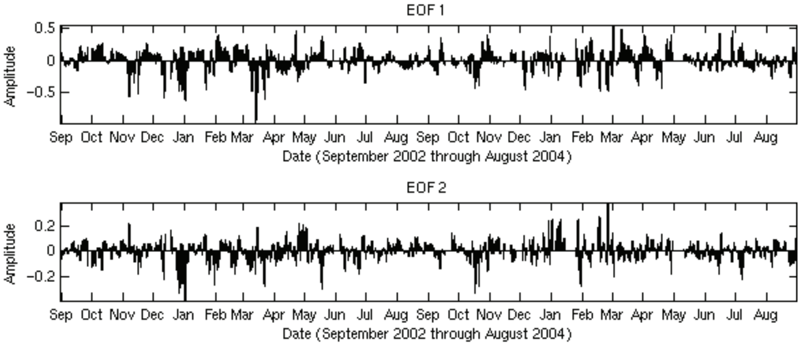

Figure 17. Time-varying amplitudes of the two most energetic EOF modes of the low-pass filtered NDBC wind stress measurements.

2.3.2 Response to Forcing

The values of the correlations between the surface current and wind-stress EOF amplitudes given in Table 2 show that the amplitude time-series of the first surface current EOF is well correlated with the first EOF of the measured wind-stress and that the second surface current EOF is well correlated with the second wind-stress EOF. Correlation between the first EOF of the surface currents and the first EOF of the wind stress is 0.83. A nontrivial correlation of 0.31 is also found between the second EOF of the surface current series and the second wind-stress EOF. The cross correlations are insignificant compared to the correlations between EOFs of the same mode.

Table 2. Lagged correlations between the first two surface current EOF amplitude time-series and the NDBC station wind-stress EOF amplitude time series. Higher EOFs were found to be uncorrelated. Lags are given in hours with negative lag meaning that the series indicated by the row is best correlated with a later point in the series specified by the column. Statistically insignificant (95% confidence) correlations are in parentheses.

	NDBC			
	EOF 1		**EOF 2**	
	corr.	lag	corr.	lag
Surface Currents				
EOF 1	0.83	1	(-0.13)	46
EOF 2	(0.17)	0	0.31	-3

The correlations between amplitude time series for the EOFs of surface current and the wind stress at individual NDBC stations (Table 3) shows that a significant portion of the variability in the surface currents is correlated with the wind stress. The first EOF of the surface currents most closely follows the forcing by τ^y and the second surface current EOF captures more of the forcing by τ^x. The EOF amplitude time-series of the first mode of the currents is strongly correlated with τ^y from all five NDBC stations with minimal lag. The strongest correlation for the surface current EOF 1 amplitudes is with τ^y at NDBC buoy 46050 at a value of 0.76. The amplitude time-series of the second EOF of the currents has its strongest correlations with τ^x from the three NDBC stations north of Cape Blanco, again with negligible lag. As for EOF 1, in EOF 2 the response of the variance in the surface currents most closely follows the forcing by NDBC buoy 46050, this time with τ^x, at a correlation of 0.44. The correlations between the wind stress time series and the surface current EOF amplitudes fall off after the second EOF, suggesting that the variance in the currents captured by these higher EOFs is not forced by the wind.

Table 3. Lag correlations between the components of the seasonal anomalies of the low-pass filtered wind stress, τ^y and τ^x (N m^{-2}), measured at the five NDBC stations and the surface current EOF amplitude time-series. Lags are given in hours with negative lag meaning that the series indicated by the row is best correlated with a later point in the series specified by the column. Statistically insignificant (95% confidence) correlations are in parentheses.

	Surface Currents					
	EOF 1		**EOF 2**		**EOF 3**	
	corr.	lag	corr.	lag	corr.	lag
τ^y						
46050	0.76	0	(0.18)	2	(0.10)	-56
NWPO3	0.67	0	0.34	2	(0.08)	-50
CARO3	0.73	0	0.34	0	(0.1)	-46
46027	0.72	-2	(0.13)	0	(0.13)	-43
46022	0.68	-3	(-0.18)	-46	(0.09)	-43
τ^x						
46050	(-0.11)	-7	0.44	4	(0.11)	0
NWPO3	(0.10)	29	0.34	4	(0.12)	-3
CARO3	0.51	5	0.43	0	(0.08)	-62
46027	-0.60	-5	(-0.07)	-2	(-0.07)	72
46022	-0.43	0	(0.22)	-7	(0.06)	7

There is a marked drop in the correlations between the wind stress from the southernmost two NDBC buoys and the amplitudes of the second EOF of the surface currents (Table 3). Since the amplitudes of the second EOF of the surface currents correlate well with τ^x at the northernmost three NDBC stations, this suggests a disconnect between the east-west component of the wind stress observed north and south of Cape Blanco. Indeed, Table 4 shows that, while there is generally good agreement between τ^x measured at the northernmost three NDBC stations and good agreement in τ^x for the two southernmost stations with each other, the correlation between the τ^x of any northern station with any southern station is poor. While this discontinuity north and south of Cape Blanco is also seen in the correlations between

τ^y, these correlations are significantly higher than that between north and south for the east-west wind stress.

Table 4. Lag correlations between the time series of the seasonal anomalies of low-pass filtered wind stress (τ^y and τ^x) measured at the NDBC stations in N m^{-2}. North-south components from each site were only correlated with the north-south components at the other sites, never with the east-west components, and vise-versa. Lags are given in hours with negative lag meaning that the series indicated by the row is best correlated with a later point in the series specified by the column. Diagonal in italics is the correlation of each series with itself. Statistically insignificant (95% confidence) correlations are in parentheses.

		46050		**NWPO3**		**CARO3**		**46027**		**46022**	
		τ^y	τ^x	τ^y	τ^x	τ^y	τ^x	τ^y	τ^x	τ^y	τ^x
46050	corr.	*1.00*	*1.00*	0.84	0.83	0.80	0.54	0.61	0.27	0.59	0.37
	lag	*0*	*0*	-1	0	-1	6	-1	-2	0	1
NWPO3	corr.			*1.00*	*1.00*	0.86	0.56	0.52	(0.17)	0.46	0.26
	lag			*0*	*0*	0	4	0	-2	2	0
CARO3	corr.					*1.00*	*1.00*	0.67	-0.26	0.61	(-0.1)
	lag					*0*	*0*	0	20	2	37
46027	corr.							*1.00*	*1.00*	0.77	0.48
	lag							*0*	*0*	2	1
46022	corr.									*1.00*	*1.00*
	lag									*0*	*0*

2.4 Discussion

2.4.1 Surface Current Seasonal Cycle

The fits to the seasonal cycle as calculated in Section 2.1 are plotted in Figures 6 and 7 for the winds and surface currents, respectively. In Figure 6 the seasonality is captured in the plot of τ^y, which has nearly the same phase at the five NDBC stations while different phases are exhibited in τ^x. In the plot of τ^y the seasonal cycle is strongest at buoy 46050, with the seasonal cycle stronger in the buoys than at the C-MAN stations on land. The timing of the spring reversal differs for stations north and south of Cape Blanco, with a shift to upwelling favorable winds occurring for those stations to the south in late March and for those stations to the north in early May. The timing of the reversal is later than that found in previous studies by about a month (Strub et al., 1987b; Kosro 2003).

The seasonal evolution of the surface currents is shown in Figure 7. The seasonal flow begins to reverse south of Cape Blanco in March with the spring transition complete by May. In May it is evident that the strongest flows are concentrated nearshore, consistent with the formation of a coastal upwelling jet. The southward velocity strengthens over the course of the summer and can be seen to move progressively offshore. In the month of July in particular, the coastal jet can be seen to separate at Cape Blanco owing to the influence of coastline topography (Barth et al., 2000).

2.4.2 Application of EOFs to Predictions

There was significant correlation between the first EOF modes of the surface currents and the wind stress along with an elevated correlation between their second EOFs (Table 2). Since these EOFs captured the highest amount of the variability in the series, this suggested that much of the seasonal anomaly of the surface currents could be predicted from the seasonal anomaly of the wind stress.

The regional dependence of the wind measurements was demonstrated by a decrease in correlations (Table 3) and a reversal in the sign of the second EOF (Figure 16) between stations north and south of Cape Blanco. This underscored the need for localized predictions of the winds, rather than generalizing the wind forcing at a single location to the current response over the entire HFR grid.

While the first EOF of the surface currents responded primarily to the alongshore wind forcing, the second EOF was forced by both components of the winds (Table 3). This necessitates a predictive model that takes into account the effect of both wind components on the surface currents.

3 Prediction of Low-pass Filtered Surface Currents Using NAM Model Forecasts of the Coastal Wind Field

As demonstrated in the previous chapter, a significant portion of the variability in the surface currents is well correlated with wind stress, as measured by coastal NDBC stations. Chapter 3 now establishes that the NAM wind forecasts represent the coastal winds sufficiently well to allow predictions of the wind-forced response of the surface currents to be made from these model winds. First, insight into the relationship between the space and time characteristics captured between the NAM model winds and surface current measurements is gained through calculation of the EOFs. A statistical model is then derived through a point-by-point bilinear regression of the NAM and surface current fields that predicts the low-pass filtered currents off the coast of Oregon up through 48 hours into the future. Finally, the statistical model is tested from March to July 2005 and the predictions are compared with surface currents measured by the HFR network.

3.1 Data Processing

NAM (formerly Eta until January 25, 2005) model forecasts have been archived at COAS starting on January 21, 2003 (Philip Barbour, COAS, *personal communication*, July 14, 2005). The NAM model produced wind analyses each day starting at 0000 UTC out until 48 hours into the future, with time-steps of three hours. Beginning February 2, 2005 forecasts began being issued out to 84 hours into the future (Environmental Modeling Center, 2005). Descriptions of the NAM model physics and its operational characteristics are given in Black (1994), Janjić (1994), and Rogers (2001). In order to analyze only those forecast hours present throughout the entire two analysis years, just the 17 forecasts issued each day from 0-h to 48-h were considered. The 10 m wind forecasts were gathered from NAM grid number 218, a 12 km Lambert conformal grid over the domain enclosed by the solid line in Figure 18.

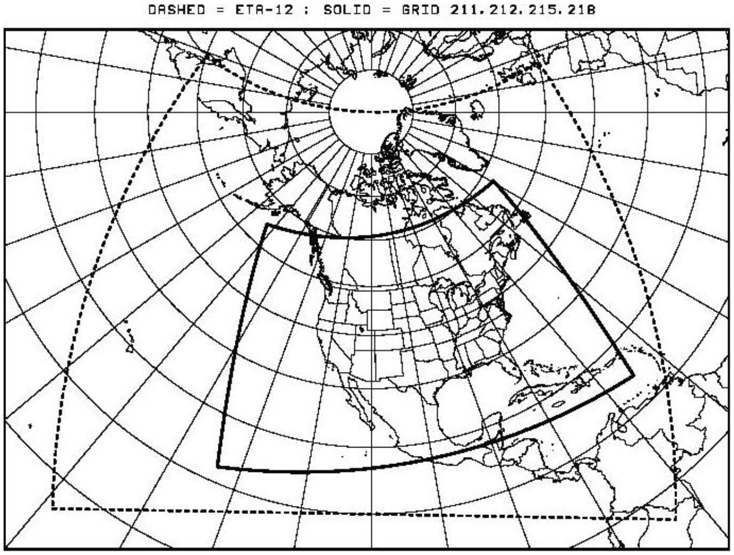

Figure 18. Domain of Lambert conformal NAM model grid #218 (solid line).

The U and V components of the daily 10 m surface wind speed forecasts were saved in World Meteorological Organization GRIB (GRIdded Binary) files (Gordon, 2002). Version 1.3.1 of Dr. Brian O. Blanton's READ_GRIB software was used to extract the 10 m wind fields (Blanton, 2005). The U and V wind speeds from the subset of the NAM grid shown in Figure 1 were then collected and transformed from Lambert conformal map coordinates into Earth coordinates using the subroutine UVMPTOE written by Dr. Keith A. Brewster, part of the ARPS software from by the University of Oklahoma's Center for Analysis and Prediction of Storms (Xue, 1995). The 10 m wind speed was then converted into τ^x and τ^y, components of wind stress in N m^{-2}, using the drag coefficients of Large and Pond (1981) modified by Trenberth et al. (1990) for low wind speeds. The wind stress was calculated in this way, rather than by directly converting the friction velocity from the NAM forecasts into stress components using surface or sea-level pressure, so that the method used to obtain τ^x and τ^y would be the same as used on the measurements of wind speed made by the NDBC stations. All the daily NAM wind forecasts of τ^x and τ^y from each forecast hour were gathered to form 17 separate two year long time series.

Since the NAM forecasts were not available at the beginning of the two year time period analyzed in Chapter 2, this necessitated the selection of a different two year time period in order to have a time-series with a balanced number of seasons and the same length as before. The forecasts over the two years from March 2003 through February 2005 were thus selected for analysis between the NAM model wind forecasts and the surface currents. There were typically a few wind analyses missing from every month, with 104 days missing in total, during the two seasonal years, including the entire month of December 2003. Measurements of the surface currents made were gathered from the same four sites as before (YHL1, WIN1, CBL1, and PSG1) over the same two years as for the NAM model data (Figure 1). As in Section 2.1, the radial measurements from each of the four sites were screened for anomalous measurements, combined into totals, and the baseline mask was applied.

Again, as in Section 2.1 *Data Processing*, the time-series at each HFR gridpoint was low-pass filtered and the seasonal cycle was extracted, forming a time-series of seasonal anomalies. The same procedure was applied to the time-series at the subset of points in the NAM grid over Oregon coastal and offshore waters (Figure 1). τ^x and τ^y at each gridpoint were low-pass filtered and then the seasonal cycle was extracted (Figure 19). The seasonal cycles and the seasonal anomalies of the time-series from all 17 forecast hours were saved.

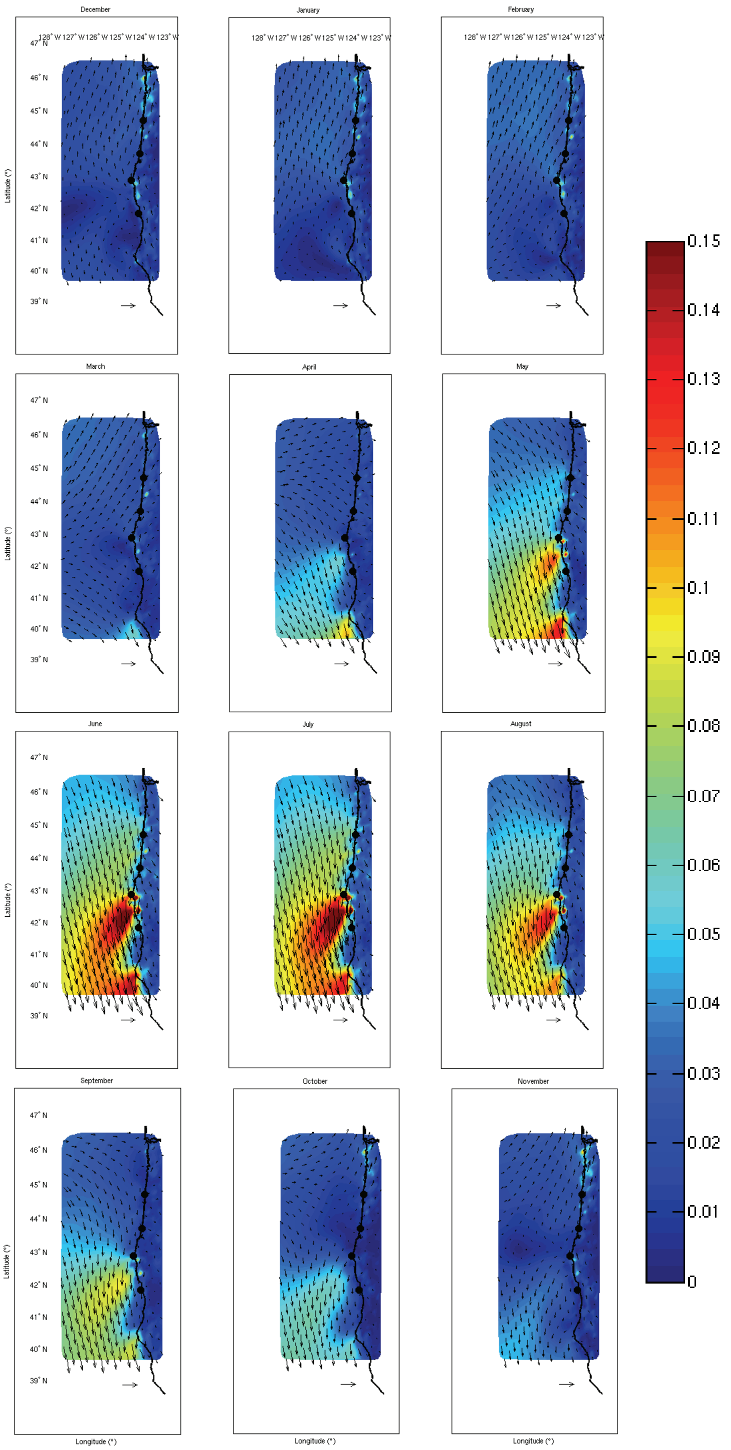

Figure 19. Fit to the seasonal cycle in the 3-h NAM data at the first of each month. 0.1 N m^{-2} scale arrows are plotted at the bottom of each panel and a black dot is placed at each HFR site along the coastline. Wind stress vectors are plotted at one-fourth density. Note how the southward shift in the winds in the month of April coincides with the formation of a coastal jet in Figure 7 during the same month.

3.2 Analysis Methods

EOF analysis was again performed as in Section 2.2 on the hourly seasonal anomalies of the low-pass filtered surface current data, this time for the two years shared by the NAM model data. The two seasonal years of NAM model data have 18 out of 24 months in common with the two years of NDBC measurements (i.e., March 2003 through August 2004 are shared). Thus the requirement that there be 1350 measurements in a given hour for that hour to be included in the surface current time-series was again used, as it had been in the analysis of the surface current series that coincided with the NDBC measurements. The threshold of 1350 measurements per hour continued to eliminate those times with the biggest drops in the HFR coverage while still preserving some hours with measurements from the winter of 2003/2004 (Figure 10). Eliminating those 2731 hours (15.6%) of the 17544 in the surface current time series without 1350 or more measurements produced a field of 930 gridpoints where data were always present (Figure 11b).

EOF analysis was also performed on the collected runs from each NAM model forecast hour. A separate EOF was calculated for the daily predictions of surface winds, processed as the seasonal anomalies of the low-pass filtered wind stress, gathered over the two years from each forecast hour. Since estimation of EOF amplitudes requires a time-series without missing data, it was necessary to omit those 104 days missing in the archives from each forecast time-series.

The U and V components of the surface current time-series were both input into MATLAB's "princomp" function as in Section 2.2 *Analysis Methods* to calculate the vector EOFs (Figures 20-22). In the same fashion τ^x and τ^y from each of the 17 NAM forecast-hour time-series were analyzed together for EOFs. Figures 23 through 25 show the results of the EOF analysis of the 3-h forecast, which is the first predictive forecast hour. Similar results were obtained from the other 16 forecast hours.

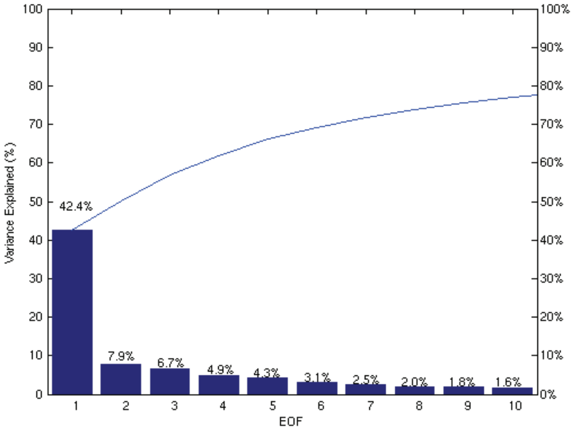

Figure 20. Percentage of the total variance in the seasonal anomalies of the low-pass filtered surface current measurements captured by each EOF mode. EOFs were calculated over the two years from March 2003 through February 2005 for the 84.5% of measurements that met the 1350 measurements per hour criterion.

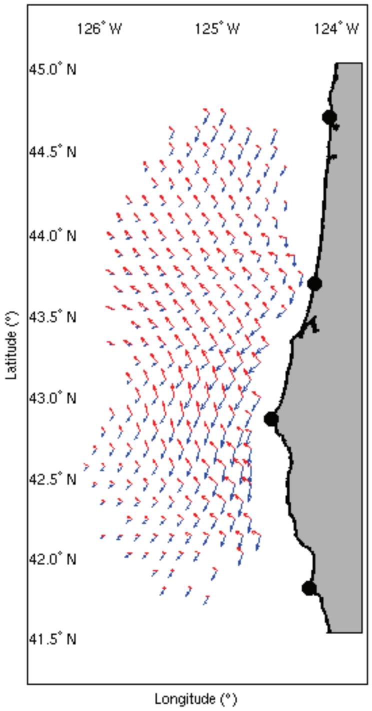

Figure 21. Shapes of the two most energetic EOF modes of the seasonal anomalies of the low-pass filtered surface current measurements. Blue is the mode shape of the first EOF; red is the mode shape of the second EOF. The magnitudes of the vectors in the EOF shapes can only be compared to one another within the same mode. The relative contribution of each EOF to the total variance is contained in the EOF amplitudes (Figure 22), rather than in the mode shapes. Black dots along the coast are HFR sites. EOF vectors are plotted at one-fourth density.

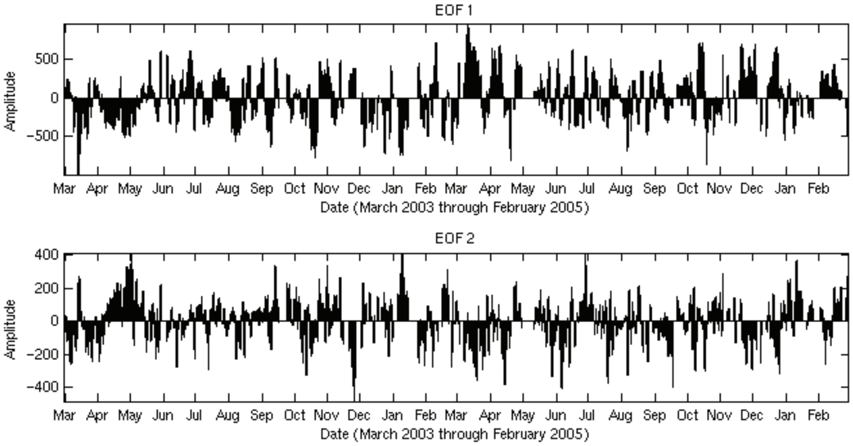

Figure 22. Time-varying amplitudes of the two most energetic EOF modes of the seasonal anomalies of the low-pass filtered surface current measurements.

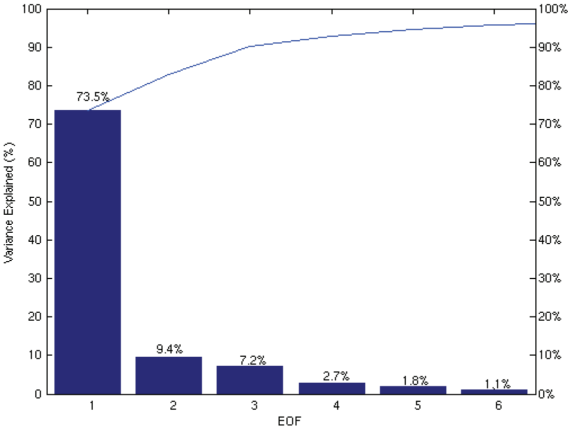

Figure 23. Percentage of the total variance in the seasonal anomalies of the low-pass filtered NAM 3-h wind stress forecasts captured by each EOF mode. EOFs were calculated over the two years from March 2003 through February 2005 for those measurements made at the same times as the measurements used in the calculation of the surface current EOFs.

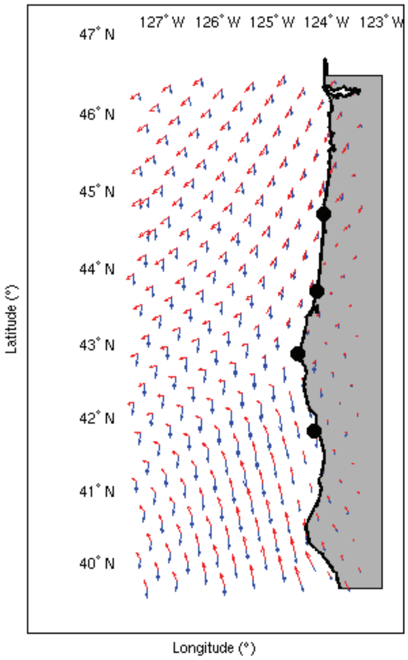

Figure 24. Shapes of the two most energetic EOF modes of the low-pass filtered NAM 3-h wind stress forecasts. Blue is the mode shape of the first EOF; red is the mode shape of the second EOF. EOFs were calculated over the two years from March 2003 through February 2005 for those measurements made at the same times as the measurements used in the calculation of the surface current EOFs. The magnitudes of the vectors in the EOF shapes can only be compared to one another within the same mode. The relative contribution of each EOF to the total variance is contained in the EOF amplitudes (Figure 25), rather than in the mode shapes. Black dots along the coast are HFR sites. EOF vectors are plotted at one-fourth density.

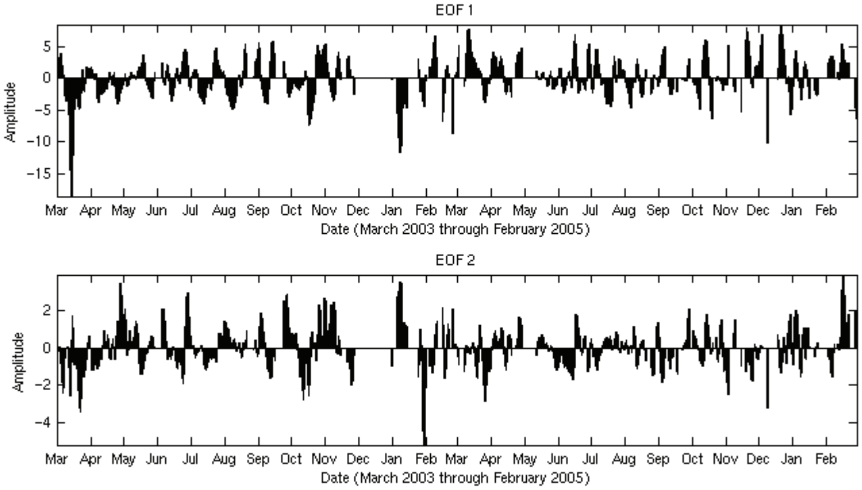

Figure 25. Time-varying amplitudes of the two most energetic EOF modes of the low-pass filtered NAM 3-h wind stress forecasts. EOFs were calculated over the two years from March 2003 through February 2005 for those measurements made at the same times as the measurements used in the calculation of the surface current EOFs.

3.3 Comparison of NAM Forecast Winds to NDBC Station Measurements

This section evaluates whether the forecasts of the winds made by the NAM model represent the coastal winds well enough to be used in predicting the wind-forced response of the surface currents off Oregon. Section 3.4 will detail the predictions and how they were made. The understanding of the modeled winds and their agreement with measurements as described in this section was necessary to have first, so that the predictions described in the next section could be made with confidence.

3.3.1 Comparison Methodology

The NAM model forecasts of the coastal winds were compared to the measurements at the NDBC stations analyzed in Chapter 2. Correlations between the NDBC wind measurements and the NAM forecasts needed to be significant and remain largely the same from the early forecast hours out until the later forecast hours if the forecasts up through 48 hours into the future were to be used to predict the response of the surface currents. The spring, summer, fall, and winter seasons from March 2003 through February 2004 were selected as the one year shared by both NAM and NDBC time series. Just the data from this one year were compared between the NDBC measurements and NAM forecasts so that no one season would be weighted more heavily than another in the comparison.

First, τ^x and τ^y from the low-pass filtered NAM fields were linearly interpolated to the locations of the five NDBC stations. Data times from the NDBC stations were matched to the forecast hours (forecasts were issued once per day). The correlation between the measured and forecast time series were calculated at zero lag for each forecast hour (Figure 26).

The same procedure as above was repeated for the seasonal anomalies of τ^x and τ^y from the NAM and NDBC series. The correlations between the seasonal anomalies of the interpolated NAM predictions from each forecast hour and the measurements made by the NDBC stations at the forecast times are plotted in Figure 27.

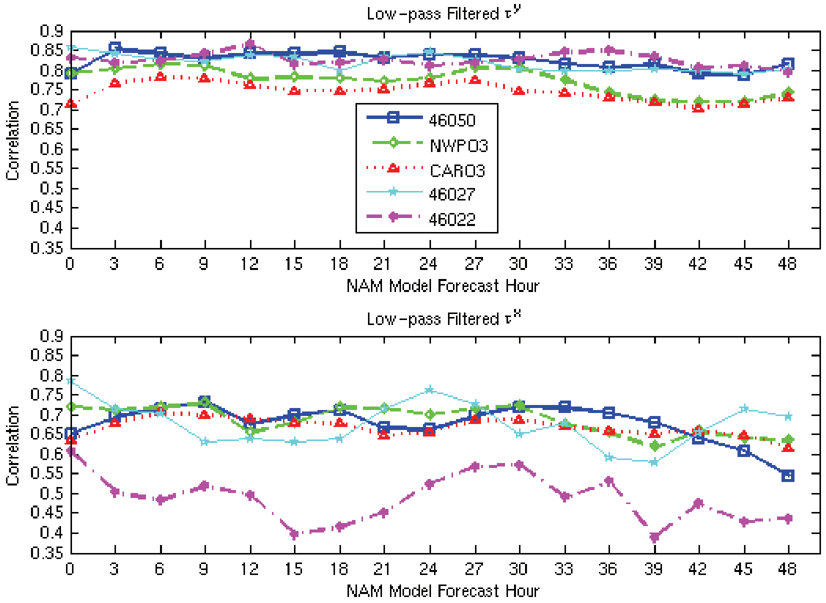

Figure 26. Correlation between the north-south (top panel) and east-west (bottom panel) low-pass filtered NDBC wind stress measurements (N m^{-2}) and the low-pass filtered NAM model wind stresses from each forecast hour. NAM model wind stresses were linearly interpolated to the NDBC station locations for those common hours over the one year from March 2003 through February 2004.

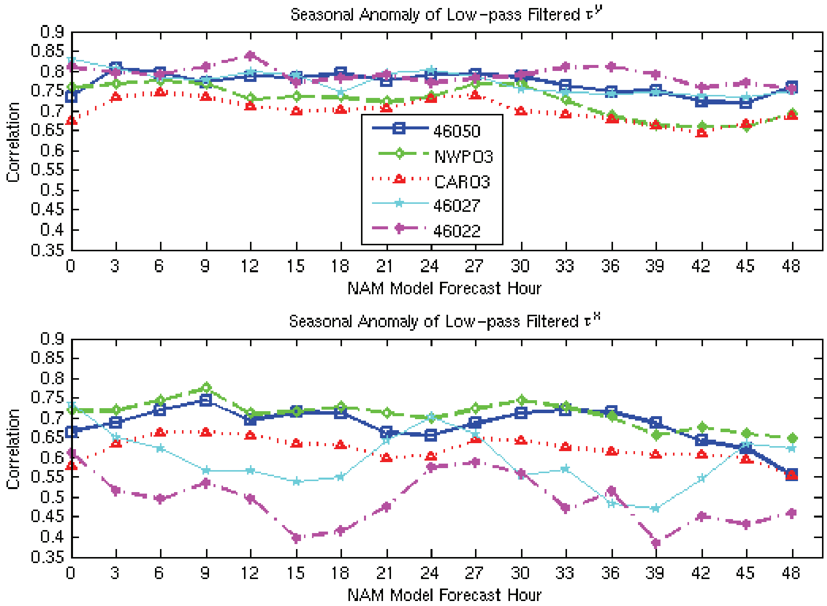

Figure 27. As in Figure 26 for the seasonal anomalies of the low-pass filtered NDBC wind stress measurements (N m^{-2}).

The seasonal cycle in the low-pass filtered NAM forecasts, subtracted to form the seasonal anomalies, was similar in all 17 forecast hour time series. The seasonal cycle in τ^x and τ^y over the one shared year was thus taken from just the time-series of the first predictive forecast hour, 3-h, and interpolated to the locations of the five NDBC stations. This interpolated NAM seasonal cycle was plotted beneath the seasonal cycle from the NDBC stations sampled to the same daily times as the forecasts (Figure 28).

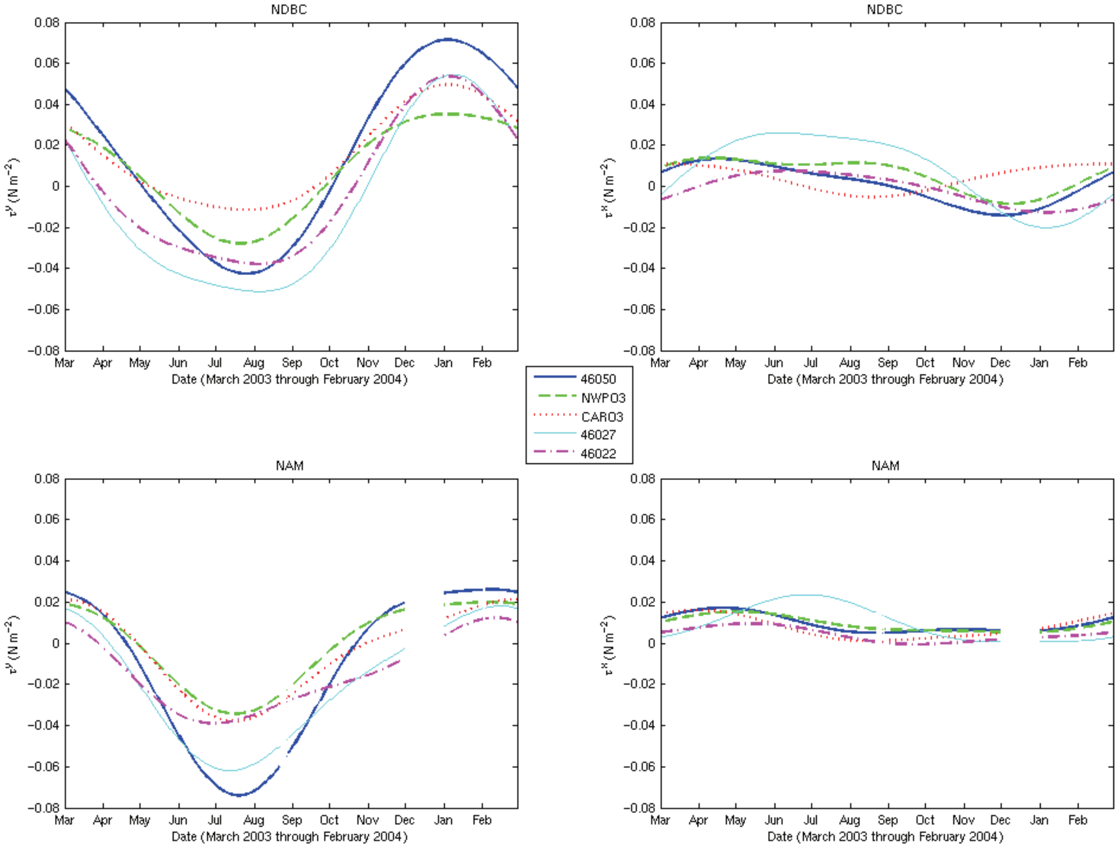

Figure 28. Seasonal cycle in the north-south (left) and east-west (right) components in the low-pass filtered wind stress measurements at the NDBC stations (top) and interpolated from the 3-h NAM forecasts (bottom). The NAM 3-h forecasts were linearly interpolated to those locations of the NDBC stations and the NDBC measurements were sub-sampled daily at 0300 UTC to match the frequency of the NAM 3-h forecasts. Gaps in the NAM model seasonal cycle represent those times where forecasts were missing.

An exception to the use of just the one shared year in the comparison of the NAM and NDBC time-series was their EOFs. It was determined that the six-month difference between the two time series would not affect the comparison of the EOF mode shapes and so the EOF analyses from Sections 3.2 and 2.2 were compared directly.

3.3.2 Results of Comparison

The seasonal anomalies of the low-pass filtered fields of τ^x and τ^y from the NAM model forecasts and NDBC station measurements remained well correlated over all 17 forecast hours (Figure 27). For model τ^y the average of the correlations with measurements the five NDBC locations at the first predictive forecast hour, 3-h, was 0.78. For those predictions of τ^y at 48-h, two days into the future, the average correlation over all five sites was 0.73. The correlation of the east-west component of the forecast winds was considerably lower than for the north-south component, with the average correlation of τ^x falling from 0.64 at 3-h to 0.57 by 48-h. Overall, the average of the correlations at all forecast hours in τ^y was 0.75 so that about 56% of the variance in the seasonal anomalies of τ^y measured by the NDBC stations is being explained by the NAM model. The overall average for τ^x was 0.62, corresponding to NAM accounting for around 38% of the measured τ^x variance.

Not including the seasonal cycle effected the correlations between the measured and forecast winds by less than 0.05, an insignificant amount (Figures 26 & 27). The reason the correlations did not decrease much was that the standard deviation of the seasonal cycle was small compared the standard deviation of the seasonal anomalies (Table 5).

Table 5. Standard deviation of the seasonal cycle and seasonal anomalies of τ^x and τ^y as measured by the NDBC stations and as forecast at 3-h by the NAM model. NDBC measurements were collected and 3-h NAM forecasts were interpolated to the five station locations over the year from March 2003 through February 2004.

Standard Deviation (N m^{-2})

NDBC

	46050		**NWPO3**		**CARO3**		**46027**		**46022**	
	τ^y	τ^x	τ^y	τ^x	τ^y	τ^x	τ^y	τ^x	τ^y	τ^x
Seasonal Cycle	0.040	0.009	0.022	0.008	0.022	0.006	0.038	0.016	0.032	0.007
Seasonal Anomalies	0.088	0.036	0.064	0.027	0.062	0.024	0.089	0.038	0.091	0.027

3-h NAM

	46050		**NWPO3**		**CARO3**		**46027**		**46022**	
	τ^y	τ^x	τ^y	τ^x	τ^y	τ^x	τ^y	τ^x	τ^y	τ^x
Seasonal Cycle	0.036	0.004	0.019	0.003	0.020	0.005	0.028	0.008	0.017	0.003
Seasonal Anomalies	0.073	0.026	0.038	0.020	0.043	0.018	0.070	0.020	0.059	0.011

The magnitude of the variance of the seasonal cycle in τ^x was about an order of magnitude smaller than in the seasonal anomalies. For τ^y the magnitude of the variance of the seasonal anomalies was more than twice that of the seasonal cycle in both the NDBC measurements and 3-h NAM forecasts (i.e., $\sigma_{\text{seasonal}} < \frac{1}{2}\,\sigma_{\text{nonseasonal}}$). Even at buoy 46050, which had the biggest fraction of variance in the seasonal cycle, $\sigma_{\text{seasonal}} \approx \frac{1}{2}\,\sigma_{\text{nonseasonal}}$, so that about 80% of the energy is nonseasonal with only 20% in the seasonal cycle.

The seasonal cycle from the NAM model was smoother than for the actual measurements, as would be expected from a mesoscale model compared to point measurements (Figure 28). This is particularly evident at CARO3 where the spring/summertime winds last from early May to mid-September in the measured winds but are cut down to mid-May through the beginning of September by the NAM model. The NAM model also had particular difficulty capturing the seasonal cycle at buoy 46050, overestimating the strength of τ^y in the summer by up to 0.3 N m^{-2} and minimizing τ^y in the winter by up to 0.5 N m^{-2}. The seasonal cycle at all locations accounted for a relatively small portion of the overall variance in the winds, in both the interpolated NAM values and as measured by the NDBC stations.

The EOF analysis of the seasonal anomalies was used to further compare the NAM forecasts and NDBC measurements. The variance and EOF mode shapes were similar between the time-series for all the NAM forecast hours, as expected from the consistency of the correlations shown in Figures 26 and 27. Figure 23 showed that the bulk of the variance in the NAM forecasts was explained in the first two EOFs, with EOF 1 accounting for 73.5% and EOF 2 9.4%. This was similar to the amount of variance explained by the first two EOFs of the NDBC measurements, 67.6% and 15.6% respectively (Figure 15). The mode shape of the first EOF in Figure 24 was alongshore everywhere, including in the region of the NDBC measurements where the first EOF was also alongshore (Figure 16). The shape of the second EOF mode of the NAM winds became more alongshore approaching the coast where the NBDC stations were located (Figure 24). This second EOF mode was alongshore close to the coast north of Cape Blanco, as it was in the second NDBC EOF mode plotted in Figure 16. The reversal of the sign for those locations south of Cape Blanco was seen in EOF 2 of both NAM and NDBC, but was not as abrupt in the NAM model results. Significant correlations were found between the time-varying amplitudes of NDBC EOF 1 and

NAM EOF 1 at around 0.7 and between NDBC EOF 2 and NAM EOF 2 at around 0.6 over all forecast hours.

3.3.3 Impact of Comparison on Prediction of Ocean Surface Currents

The NAM model's predictions were consistent in their accuracy with minimal deterioration in skill out through two days into the future. The NAM wind forecasts accounted for the majority of the variance in the NDBC measurements of τ^y, the north-south component of the wind stress, which was shown to exert the greatest influence on the surface current response. The predictions by the NAM model of τ^x, which along most areas of the coast represented the cross-shore wind, were also reasonably well correlated with the measured winds at around 0.6 (Figure 27). In addition to τ^y being a larger component of the wind signal than τ^x, the north-south component of the winds encounters a roughly parallel north-south coastline over the extent of the domain (with the most notable exception being at Cape Blanco). The coastal orography encountered by the cross-shore winds is considerably more complex (National Center for Atmospheric Research, 1998). The more localized, shorter scale response of τ^x to these features would be captured in the record of the buoy winds but would be smoothed by the step-mountain implementation of topography used in the NAM model (Gallus, 2000).

The EOF mode shapes of the NAM forecasts and NDBC measurements varied similarly in space. The change in the sign of the second EOF at Cape Blanco, seen in both the NDBC winds and the surface currents, was picked up in the wind predictions of the NAM model. Given the agreement of the NAM forecasts of the wind stress with the *in situ* measurements over a one year comparison period, it was determined that the NAM model winds would be used to predict the response of the surface currents off the Oregon coast.

3.4 Predicting Low-pass Filtered Surface Current Fields off the Oregon Coast Using HFR Measurements and NAM Model Wind Forecasts

The low-pass filtered surface current fields were considered to have three predictable parts. The first were the seasonal anomalies which, as shown in this section, could be predicted with some skill from the wind-forced response to the NAM forecasts. The second part was the seasonal cycle which, per Section 3.1, was defined at all times during the year. The third part was the residual difference between the latest detided surface current measurements and the sum of the predicted seasonal anomalies and seasonal cycle.

For vector surface currents $\vec{u}$ at point $\vec{x}_i = (x_i, y_i)$ with i the gridpoint number and time t_n with n as the forecast hour

$$\vec{u}(\vec{x}_i, t_n) = \vec{u}_{\text{wind anomaly}}(\vec{x}_i, t_n) + \vec{u}_{\text{seasonal}}(\vec{x}_i, t_n) + \vec{u}_{\text{residual}}(\vec{x}_i, t_n) \qquad \text{(Eqn. 1)}$$

where

$\vec{u}_{\text{wind anomaly}}$ is determined from regression on the local predicted wind at that time,

$= \vec{\alpha}_n(\vec{x}_i)\cdot\tau^{x}_{\text{NAM}}(\vec{x}_i, t_n) + \vec{\beta}_n(\vec{x}_i)\cdot\tau^{y}_{\text{NAM}}(\vec{x}_i, t_n) + \vec{\gamma}_n(\vec{x}_i)$ (Eqn. 1a), where slopes $\vec{\alpha}$ and $\vec{\beta}$, as well as the constants $\vec{\gamma}$, are functions of $\vec{x}_i$.

$\vec{u}_{\text{seasonal}}$ is based on a fit to the measured surface current data at each location.

$\vec{u}_{\text{residual}}(\vec{x}_i, t_n) = \vec{u}_{\text{measured}}(\vec{x}_i, t_{av_1}) - \lfloor \vec{u}_{\text{wind anomaly}}(\vec{x}_i, t_{av_2}) + \vec{u}_{\text{seasonal}}(\vec{x}_i, t_{\text{-1200 UTC}}) \rfloor$ (Eqn. 1b) representing the part of the current that is not correlated with local wind, such as eddies. Time scales of several days are assumed for these residual components. t_{av_1} indicates the average of the surface current measurements ($\vec{u}_{\text{measured}}$) over the 24 hours leading up to 0-h (i.e., -2400 UTC through 0000 UTC). t_{av_2} indicates the average of $\vec{u}_{\text{wind anomaly}}$ calculated at 0000 UTC and at 0000 UTC from the day before.

The seasonal anomalies of low-pass filtered surface currents ($\vec{u}_{\text{wind anomaly}}$) were predicted from Eqn. 1a, a point-by-point bilinear regression with the seasonal anomalies of the low-pass filtered NAM wind forecasts (see Section 3.4.1). The seasonal cycle of the low-pass filtered surface currents at each point in the HFR grid ($\vec{u}_{\text{seasonal}}$) was defined by the time of the forecast using the harmonic fit calculated in Section 3.1 and, when added to $\vec{u}_{\text{wind anomaly}}$, produced a prediction of the low-pass filtered surface currents. In Eqn. 1b the 0-h prediction of the low-pass filtered surface currents ($\vec{u}_{\text{wind anomaly}}(\vec{x}_i, t_{0000\,\text{UTC}})$) was averaged with the 0-h prediction from the day before ($\vec{u}_{\text{wind anomaly}}(\vec{x}_i, t_{-2400\,\text{UTC}})$) then, along with the seasonal cycle at the time of the mean, subtracted from detided surface current measurements, thereby creating a residual ($\vec{u}_{\text{residual}}$) to account for the error in the prediction (see Section 3.4.2). $\vec{u}_{\text{residual}}$, carried through all the forecast hours, completed the prediction of the low-pass filtered surface currents out until 48 hours into the future.

3.4.1 Prediction of Seasonal Anomalies of Low-pass Filtered Surface Currents using Bilinear Regression

To form the time-series for the bilinear regressions it was first necessary to linearly interpolate the daily fields of τ^x and τ^y in each forecast hour's two year time-series to the locations of the HFR gridpoints (Figure 1). Then the U and V surface current measurements taken at the times of the forecasts during the two-year analysis period were gathered. MATLAB's "regress" function was used to form 17 bilinear regressions, $\vec{\alpha}_n(\vec{x}_i) \cdot \tau^x_{\text{NAM}}(\vec{x}_i, t_n) + \vec{\beta}_n(\vec{x}_i) \cdot \tau^y_{\text{NAM}}(\vec{x}_i, t_n) + \vec{\gamma}_n(\vec{x}_i)$; one between the time-series of interpolated τ^x and τ^y wind stress components from each forecast hour, n, and the U and V surface currents at each gridpoint, i. The results are shown in Figure 29 for the first predictive forecast hour n=3 (i.e., 3-h). The spatial structure of the slopes and intercept shown in Figure 29 were similar to the results obtained from the regressions of the time-series at the other forecast hours.

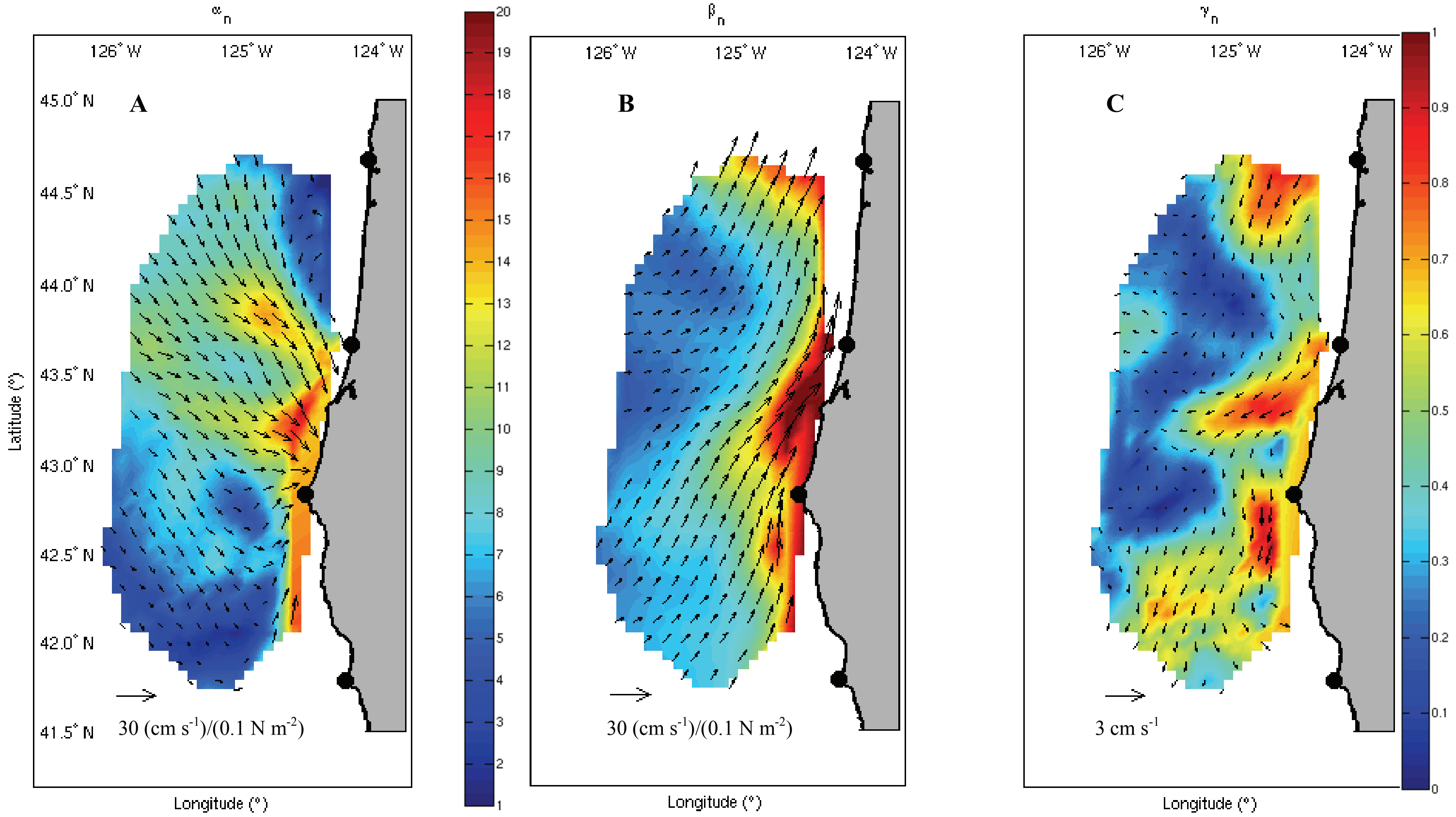

Figure 29. Bilinear regressions, calculated as a function of location, between the two-year time-series of surface currents (cm s^{-1}) and NAM wind stress (N m^{-2}) at forecast hour 3-h. The slopes of the regression plotted in panels A and B show the increase in current per 0.1 N m^{-2} increase in zonal and meridional wind stress, respectively. Panel C is the intercept of the regression (cm s^{-1}), showing the predicted surface current in the absence of wind stress. Panels A and B share the colorbar between them with units of (cm s^{-1})/(0.1 N m^{-2}) and panel C has its own colorbar to the right with units of cm s^{-1}. Scale arrows for the slopes and intercept indicate 30 (cm s^{-1})/ (0.1 N m^{-2}) and 3 cm s^{-1}, respectively.

The first slope of the bilinear regression, $\vec{\alpha}_n(\vec{x}_i)$, gave the spatially dependent response of both the U and V components of the surface currents to a variation in the zonal wind stress (Figure 29A). The other slope from the bilinear regression, $\vec{\beta}_n(\vec{x}_i)$, also gave the spatially dependent response of the vector surface currents but to a variation in the meridional wind stress (Figure 29B). $\vec{\gamma}_n(\vec{x}_i)$ is the intercept, giving the expected current in the absence of wind stress (Figure 29C).

In order to take the 10 m U and V wind speeds from incoming NAM forecasts from outside the two-year analysis period and use the bilinear regressions to make future predictions, the wind speeds had to be transformed into seasonal anomalies of low-pass filtered wind stress. This was done for a given day's 17 forecasts by repeating the processing described in Section 3.1. The value of the seasonal cycle that day from the 17 fits (one for each forecast hour, previously calculated over the two-year analysis period) was then subtracted. With the day's NAM forecasts now seasonal anomalies of low-pass filtered wind stress, the values were linearly interpolated to the HFR gridpoints. Once this was done, τ^x and τ^y could be converted into the U and V components of the seasonal anomalies of the low-pass filtered surface currents, $\vec{u}_{\text{wind anomaly}}$, using the values from the bilinear regression,

$\vec{\alpha}_n(\vec{x}_i)\cdot\tau^x_{\text{NAM}}(\vec{x}_i,t_n)+\vec{\beta}_n(\vec{x}_i)\cdot\tau^y_{\text{NAM}}(\vec{x}_i,t_n)+\vec{\gamma}_n(\vec{x}_i)$.

Justification for using both the τ^x and τ^y components of the forecast winds in Eqn. 1a to predict each the U and the V surface currents was given in Table 3. The majority of the variability in the EOFs, which describe the surface current wind anomalies, was correlated with both the τ^x and τ^y components of the seasonal anomalies of the low-pass filtered winds (Sections 2.3.2 & 2.4.2). Even though the magnitude of the τ^y component of the winds was considerably larger than that of τ^x (Figures 8 & 9), forcing by τ^y alone could thus not be used to predict the surface current wind anomalies. Another method utilizing EOFs to predict the response of the surface currents to the winds was formulated and examined prior to settling on the use of bilinear regressions to predict $\vec{u}_{\text{wind anomaly}}$, but the bilinear regressions turned out to be less computationally intensive and conceptually simpler while also being more accurate (Appendix B).

3.4.2 Addition of Seasonal Cycle and Calculation of Residual

With $\vec{u}_{\text{wind anomaly}}$ now defined, the remaining terms were calculated by adding back the seasonal cycle and comparing the predictions to recent measurements made by the HFR surface current mappers. $\vec{u}_{\text{residual}}$ was calculated from the difference between the mean of the surface currents over t_{av_1} and the average of $\vec{u}_{\text{wind anomaly}}$ over t_{av_2} plus $\vec{u}_{\text{seasonal}}$.

To filter out tidal variations, $\vec{u}_{\text{measured}}$ were averaged over t_{av_1}, creating a measured value centered at -1200 UTC, 12 hours prior to the day's 0000 UTC forecast. Likewise, the $\vec{u}_{\text{wind anomaly}}$ values calculated for yesterday and today's analysis hour were averaged, t_{av_2}, to create a mean value centered at -1200 UTC. The seasonal cycle at -1200 UTC, $\vec{u}_{\text{seasonal}}(\vec{x}_i, t_{\text{-1200 UTC}})$, was computed from the harmonic fit over the two year analysis period and added to $\vec{u}_{\text{wind anomaly}}(\vec{x}_i, t_{av_2})$ to produce a prediction of the low-pass filtered surface currents at the time of the most recently available detided measurement.

$\vec{u}_{\text{residual}}(\vec{x}_i, t_n)$ was added to the prediction at each forecast hour to correct for the difference between the measured surface currents and the surface currents predicted from the wind-driven response alone. This residual decorrelated over time since it represented a difference between the measurements and the predictions 12 hours prior to 0-h; by 48-h this residual was effectively 60 hours old.

The final step was to add the seasonality to the surface current predictions. The seasonal cycle calculated from the two years of surface current data was referenced for those values defined at the times of the forecasts, t_n. $\vec{u}_{\text{seasonal}}(\vec{x}_i, t_n)$ was added to $\vec{u}_{\text{wind anomaly}}(\vec{x}_i, t_n)$ along with $\vec{u}_{\text{residual}}(\vec{x}_i, t_n)$, creating values at each red point shown in Figure 11b of low-pass filtered surface currents $\vec{u}(\vec{x}_i, t_n)$.

3.4.3 Predictions and Results

The statistical model derived from the regressions of Eqn. 1a (as well as the EOF model in Appendix B) was tested on 117 days between March 2, 2005 and July 10, 2005 to encompass all available data not included in the model setup; thus the test period only included spring and summer data (as was typical of the NAM archives kept at COAS, there were days missing from each month).

The forecast hours 3-h, 24-h, and 48-h were chosen out of the 17 to represent the results of the predictions for the sake of compactness. The analysis hour is not shown because the NAM model winds at 0-h, from which the surface current predictions are derived, represent observations along with a set of initial conditions in a trial field and thus are not true forecasts (University Corporation for Atmospheric Research, 2002).

Figure 30 compares a time-series of the V low-pass filtered surface current measurements made at a point off the Oregon coast with the predictions from the sum $V(y_i, t_n) = V_{\text{wind anomaly}}(y_i, t_n) + V_{\text{seasonal}}(y_i, t_n)$ (i.e., not including the residual term from Eqn. 1c).

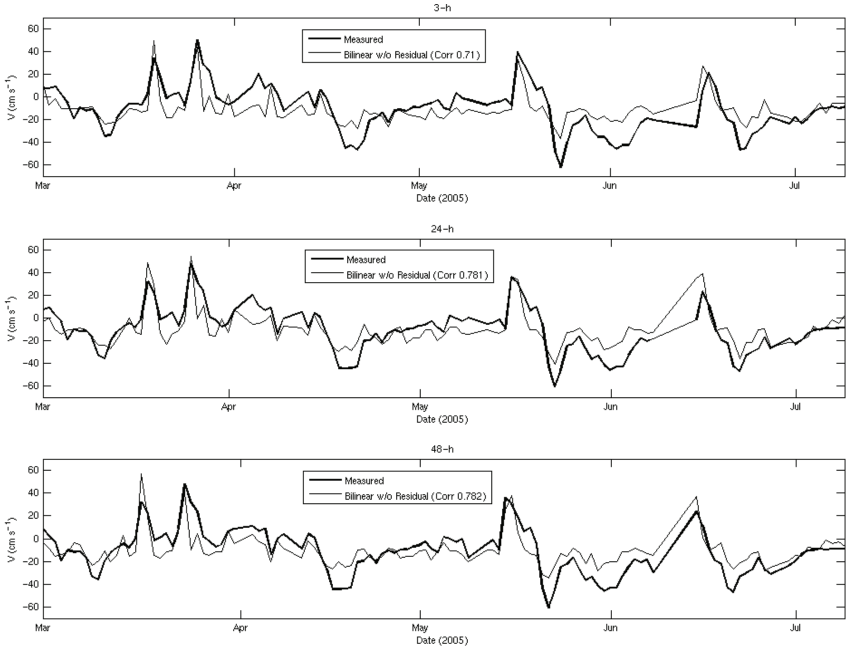

Figure 30. Time-series of the V component of the low-pass filtered surface currents at gridpoint 42° 58' 25" N, 124° 39' 52" W over the 177 days where predictions were made. Bold line is measured surface currents and the thin line is the result of the prediction using bilinear regression, without the residual component. Correlations between the measurements and the results for the forecast hours at this point are given in the legends.

Since the surface currents measured at 0300 UTC on each of these 117 days are not the same as those measured at 0000 UTC the following day or 0000 UTC two days into the future, the time-series of the measurements and predictions at the three forecast hours are not the same. The bilinear regressions alone are able to track the changes in the detided surface currents based on only the seasonal-anomalies of the low-pass filtered wind stress and the seasonal cycle. There was consistent correlation at this point in excess of 0.7 out through 48 hours into the future. In Figure 31,

$V(y_i, t_n) = V_{\text{wind anomaly}}(y_i, t_n) + V_{\text{seasonal}}(y_i, t_n) + V_{\text{residual}}(y_i, t_n)$, whereby the effect of adding the residual is seen.

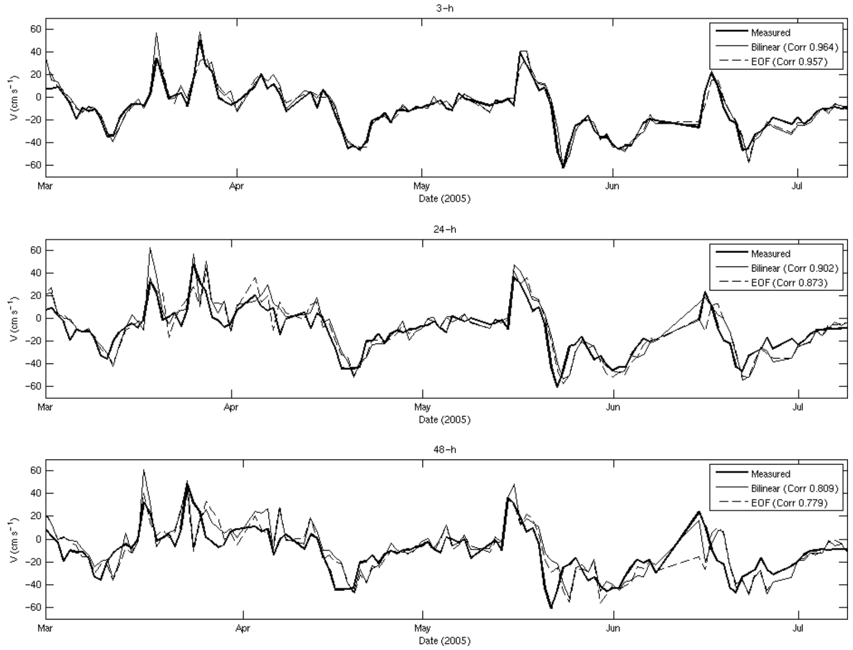

Figure 31. Time-series of the V component of the low-pass filtered surface currents at gridpoint 42° 58' 25" N, 124° 39' 52" W over the 177 days where predictions were made. Bold line is surface currents measured by HFR. The thin lines are the results of the predictions using bilinear regression, and the dashed lines are the results of the predictions using EOFs (Appendix B). Correlations at zero lag between the measurements and the results of the predictive schemes at this point are given in the legends.

The correlations are boosted out through 48 hours into the future, but the benefit of the residual is most impressive in the earlier forecast hours when the part of the surface currents uncorrelated with the forecast winds has had the least time to change. Even with the aid of the residual, the predictions made using the EOF model in Appendix B are less accurate than the results of the bilinear regressions. While the level of correlation with the particular measurements is location-specific, the difference seen in the skill between the EOF model and the bilinear regressions is representative of points throughout the grid.

Figures 30 and 31 showed comparisons at just one point. To assess the overall performance of the surface current predictions, the skill at all the HFR gridpoints will be examined. Correlations were calculated between each prediction, $\vec{u}(\vec{x}_i, t_n)$, its components, $\vec{u}_{\text{wind anomaly}}(\vec{x}_i, t_n)$, $\vec{u}_{\text{seasonal}}(\vec{x}_i, t_n)$, and $\vec{u}_{\text{residual}}(\vec{x}_i, t_n)$, and the time-series of low-pass filtered surface current measurements over the 117 days. Figure 32 shows the results of these calculations for the time-series of 3-h, 24-h, and 48-h forecast hours.

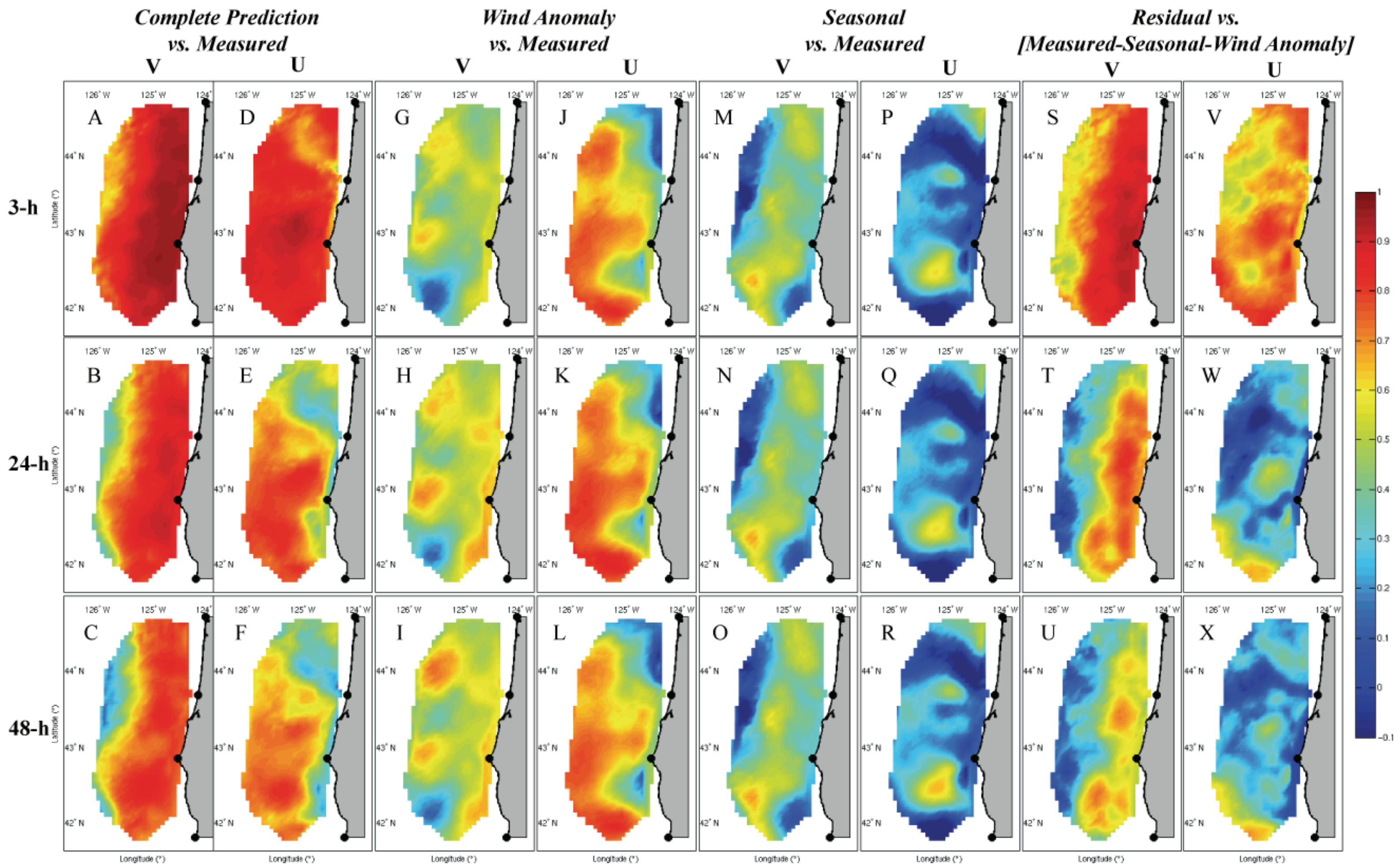

Figure 32. Correlations at zero lag between surface current measurements over the 117 forecast days and the components of the predictions. Row labels are the forecast hour. Column labels specify the forecast component.

The greatest persistence in the residual can be seen alongshore in the V component of the currents (Figures 32S-32T), perhaps owing to the predominance of the coastal jet in the currents off of Oregon (Kosro, 2005). The V component of the seasonal cycle (Figures 32M-32O) also explains more of the measured signal than does the U component (Figures 32P-32R), except in the region offshore south of Cape Blanco centered around 42º 27' N, 125º 15' W. Correspondingly, the wind-driven predictions of the seasonal anomaly in U calculated from the bilinear regressions (Figures 32J-32L) show a drop in correlation around 42º 27' N, 125º 15' W. Otherwise the wind-driven predictions for U correlate well, generally greater than 0.6, in the regions offshore. The seasonal cycle accounts for more of the signal in V (Figures 32M-32O) than it does in U (Figures 32P-32R), so the correlations for the V component of the wind-driven seasonal anomalies (Figures 32G-32I) are not as high as for the U component (Figures 32J-32L). The correlations of the wind-driven V component with the measurements are more consistent throughout the map than U, however, and, save for the region in the southwest corner of the field, are generally greater than 0.5. The total predictions are particularly good at the first predictive forecast hour, 3-h (Figures 32A & 32D), since the residual is only 15 hours old for these forecasts. The correlations with the residual components alone (Figures 32S & 32V) show that the surface currents do not change much over 15 hours, but at the 48-h forecasts when the residual signal is 60 hours old, it has faded considerably (Figures 32U & 32X).

The amount of the covariance in the measured signal accounted for by the three forecast components, $\vec{u}_{\text{wind anomaly}}(\vec{x}_i, t_n)$, $\vec{u}_{\text{seasonal}}(\vec{x}_i, t_n)$, and $\vec{u}_{\text{residual}}(\vec{x}_i, t_n)$, is shown in

Figure 33. To produce these plots the covariance between the measurements and predictions was divided by the autocovariance in the measurements themselves and multiplied by 100. The plots in Figure 33 show that the wind-driven predictions of the seasonal anomalies account for the bulk of the predictive skill in the model (Figures 33C & 33F) as the residual signal fades (Figures 33O & 33R). The influence of the seasonal cycle remains restricted to essentially two regions in the southwest and northern portions of the field (Figures 33V-33U). The amount of the measurements accounted for by the residual faded after around a day (Figures 33N & 33Q) but still remained relevant for regions alongshore, particularly in V out to the 48-h forecast (Figure 33O).

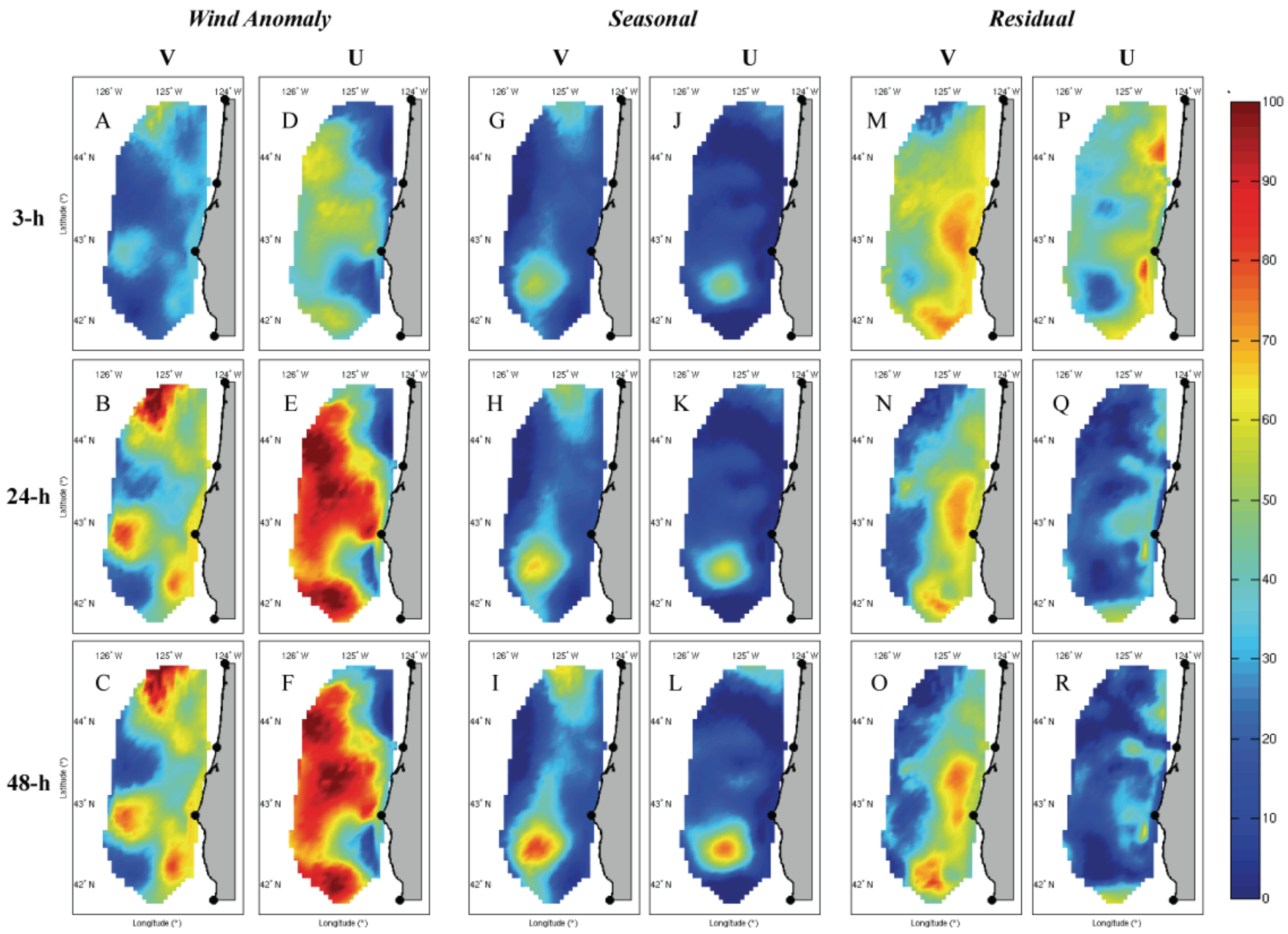

Figure 33. Percentage of the covariance in the measured surface currents accounted for over the 117 forecast days by each of the three forecast components. Row labels are the forecast hour. Column labels specify the forecast component.

A description of the error in the 117 days of complete predicted surface currents, $\vec{u}(\vec{x}_i, t_n) = \vec{u}_{\text{wind anomaly}}(\vec{x}_i, t_n) + \vec{u}_{\text{seasonal}}(\vec{x}_i, t_n) + \vec{u}_{\text{residual}}(\vec{x}_i, t_n)$, is given by Figure 34. The seasonal cycle, wind-driven, and residual components of the surface current predictions were added to form complete forecasts. Low-pass filtered measurements of the surface currents were then subtracted from these low-pass filtered surface current forecasts to yield the error. The mean and standard deviation of the error at each gridpoint were then plotted for both the V and U components at the 3-h, 24-h, and 48-h forecast hours. The standard deviations of the errors made by the predictions (panels 33I-33N) were highest in those same areas where the standard deviations of the measurements themselves were high (Figures 34O & 34P). The low standard deviation in the 3-h predictions (Figures 34I & 34L) was due to the high persistence of the residual component at only 15 hours old (Figures 32S & 32V) with a notable exception in the U component of the surface currents west of Coos Bay, Oregon. As the surface currents were forecast farther into the future, the error in the V component (Figures 34A-34C) developed into a distinct alongshore band in the region of the alongshore jet during these spring and summer months (Figure 7). The largest errors in the U component at the 24-h and 48-h forecast hours were found north of Cape Blanco, in the same region where the greatest intensity was found in the coastal jet (Figure 7).

Figure 34. Mean difference (A-F) and standard deviation (I-N), both in cm s^{-1}, of the predicted values in the complete forecast and the measured surface currents. Labels V and U above the columns indicate the meridional and zonal components, respectively. Labels to the left of the rows indicate the forecast hour of the panels in row. Included as panels G and H are histograms of the mean errors in V and U. The histograms justify limiting the mean difference color scale to values between -1 and 4 cm s^{-1}. The standard deviation of the time-series of the measured surface currents is plotted in O and P. The error colorbar on the left side of the page is for A-F and the standard deviation colorbar on the right is for I-P.

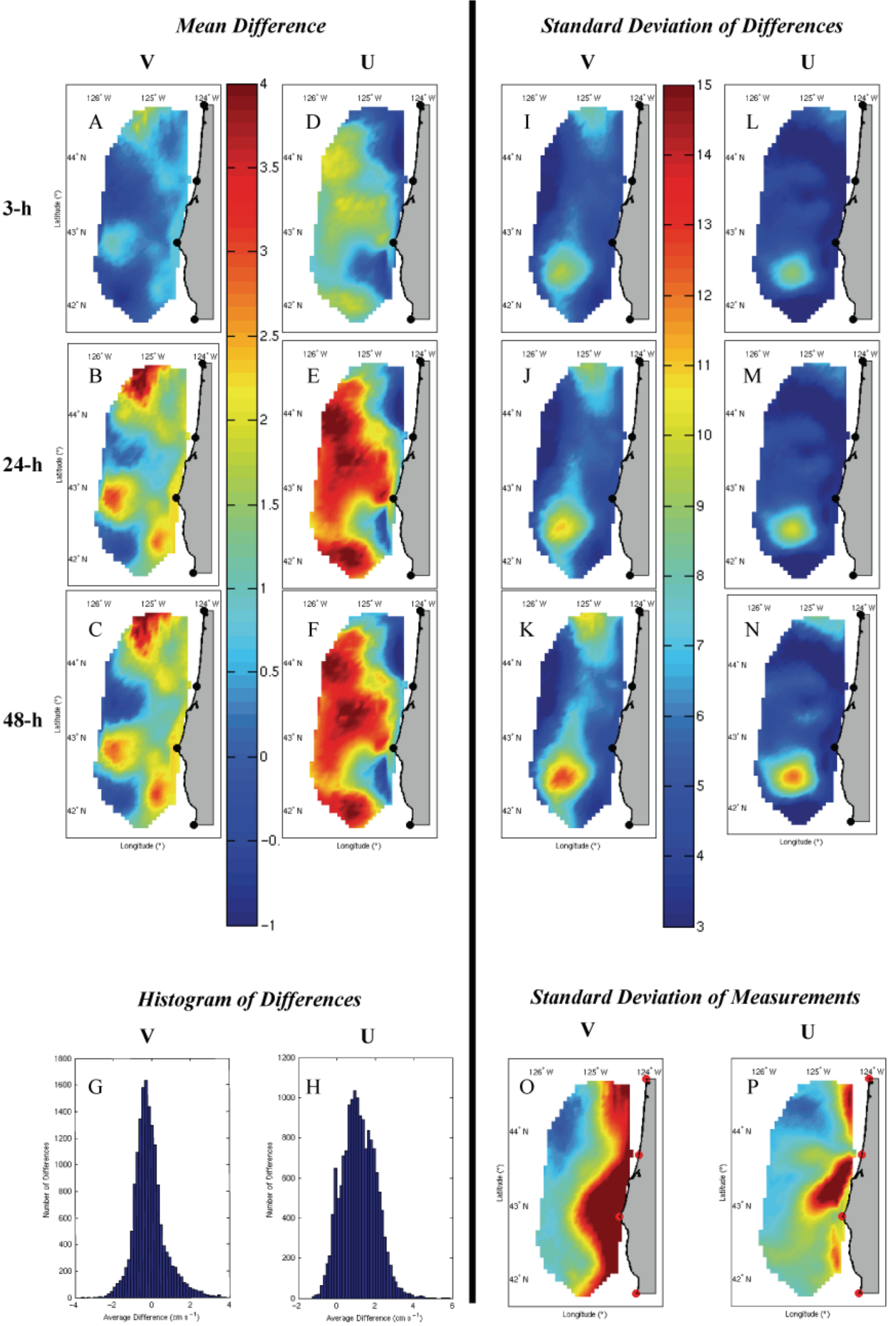
Mean Difference
V
U
Standard Deviation of Differences
V
U
3-h
24-h
48-h
A
B
C
D
E
F
I
J
K
L
M
N
126° W
125° W
124° W
44° N
43° N
42° N
Latitude (°)
Longitude (°)
4
3.5
3
2.5
2
1.5
1
0.5
0
−0.
−1
15
14
13
12
11
10
9
8
7
6
5
4
3
Histogram of Differences
V
U
G
H
Number of Differences
Average Difference (cm s⁻¹)
Standard Deviation of Measurements
V
U
O
P

Figure 34.

3.5 Discussion

In Chapter 2 the seasonal anomalies of the low-pass filtered surface currents were shown to be correlated with measurements of the wind using EOF analysis, a result also seen for wind predictions derived from NAM over large areas off the coast (Figures 32 & 33). This suggests that the NAM model has skill in forecasting the winds off the Oregon coast in more places than at just the NDBC stations. The variation in the winds seen at the relatively closely spaced NDBC stations demanded a model that could capture the changes in the coastal wind field in detail (Figures 6, 8, & 9). The 12 km mesoscale resolution of the NAM model proved a good fit to this requirement and allowed interpolation of the forecast winds down to the 6 km resolution of the surface current measurements.

The impact of both the north-south and east-west components of the wind stress on the surface currents dictated the use of a statistical model that relied on both of these components. The bilinear regressions (Eqn. 1a) satisfied this requirement by predicting the U and V currents from both the τ^y and τ^x components of the low-pass filtered seasonal anomalies of the forecast wind stress. The maps of the vector responses to either a northward or eastward wind stress indicate response in the direction of the wind and to the right of the wind over the largest portion of the map (Figure 29).

In Figure 29B, $\vec{\beta}_n$ is positive everywhere so that when forecast τ^y is southward, the predicted seasonal anomalies of the low-pass filtered surface currents increase southward and offshore everywhere (and likewise for northward τ^y, with a northward and onshore current response). The magnitude of the surface current response to τ^y is highest alongshore, in the region of the coastal jet. The direction of the seasonal anomalies of the low-pass filtered surface currents also vary across the map in response to τ^y, becoming more meridional towards shore, reaching a maximum in the same regions where the current jet was strongest in the summer in the seasonal cycle of the surface currents (Figure 7).

The slope $\vec{\alpha}_n$ plotted in Figure 29A indicates a predominantly onshore and southward flow in response to eastward forcing by τ^x. There is an approximately twofold change in the magnitude of the response of the seasonal anomalies of the low-pass filtered surface currents, from around 10 (cm s^{-1})/(0.1 N m^{-2}) north of Cape Blanco to 5 (cm s^{-1})/(0.1 N m^{-2}) to the south.

The intercept of the bilinear regressions, $\vec{\gamma}_n$ (Figure 29C), show that in the absence of a forecast wind stress, the seasonal anomalies of the low-pass filtered surface currents retain a portion of the alongshore coastal jet. Additionally, in those regions where $\vec{u}_{\text{wind anomaly}}$ predicted the least amount of the measured covariance in the V component of the surface currents (Figures 33A-33C), there is a corresponding increase in the magnitude of the intercept (Figure 29C).

The results of the regressions shown in Figures 29B and 29C were similar to those presented in Kosro (2005) for comparisons of the surface currents with the τ^y component of measured winds. Kosro (2005) used standard-range CODAR SeaSondes to measure the surface currents, rather than the long-range SeaSonde systems used here, so their measurement region extended from 44.1° N to 45.1° N between 124.1° W to 124.5° W with a higher 2 km resolution. Like in Figure 29B, Kosro (2005) found the regression between the surface currents and τ^y to be positive everywhere. Kosro (2005) also found the intercept of the linear regression captured a remnant of the alongshore current jet, similar to what was presented in Figure 29C.

A linear fit to the time-varying amplitudes of the vector EOFs, derived from both the east-west and north-south components of the NAM winds and the surface currents, was also formulated (Appendix B). While both of the bilinear and EOF statistical models were effective, the relative conceptual simplicity and predictive accuracy of the bilinear regressions proved superior (Figure 31).

The predictions of the empirical statistical model derived from the bilinear regressions evaluated over the 117 days demonstrated spatial as well as temporal variability in the quality of the results (Figures 32-34). The addition of the seasonal cycle to the seasonal anomalies predicted by the bilinear regressions (Eqn. 1a) produced a low-pass filtered surface current field with skill in and of itself (Figure 30) but when recent measurement from HFR surface current mappers were projected into the future via the residual term (Eqn. 1b), the predictions improved considerably (Figure 31). This enhancement of the forecast by the residual was, by definition, greatest in the earlier forecast hours (Figure 32).

These complete predictions showed strong correlation with measurements of the surface currents. The predictions 24 into the future were correlated with measurements all along the coast in V and largely for those locations south of WIN1 in U at values greater than 0.8 (Figures 32B & 32E). The correlations remained in excess of 0.7 in both the U and V components for forecasts up through 48 hours into the future, over large areas of the domain (Figures 32C & 32F). Looking at the contribution of each component to the forecast, it was clear that the relative importance of each piece of the prediction varied throughout the map (Figures 32 and 33). The wind-driven currents, $\vec{u}_{\text{wind anomaly}}$, were most reliable in those regions where the seasonal cycle exerted little influence (Figures 32G-32L & Figures 33A-33L). The residual was most persistent in the region of the coastal jet (Figures 32S-32X & Figures 33M-33R). The largely southerly flow in the jet region throughout the entire summer (Figure 7) explained the persistence of the V component of the residual over at least 2.5 days.

The error in the predictions largely followed the measured variability in the surface currents and additionally seemed to be influenced by shoreline topography at Cape Blanco (Figure 34). As was discussed in Section 3.3.3, some of this regionalized error may be the result of the simplified orography used in the NAM model leading to over-smoothing of local features.

3.5.1 Case in "Point"

Among the uses for forecasts of surface currents would be predicting the location of a drifting object. To do this out on the ocean would require knowing not only the low-pass filtered currents predicted by this model, but also the tidal currents not included in these forecasts. Nonetheless, it is possible to get a sense of the amount of uncertainty in this low-pass filtered portion of the currents that would be removed by having these predictions.

The same point (42° 58' 25" N, 124° 39' 52" W) as considered in Figures 30 and 31 was selected to test the contribution of each forecast component. The average of the U and V correlations between the 6-h predictions and measurements at that point over the 117 forecast days was 0.91. The U and V components of the measurements were combined to yield the velocity at that point, which over the 117 days had a standard deviation of 14.1 cm s^{-1}. If an object were considered to travel at the rate of the standard deviation, then it would have traveled up to 3.05 km from that point in six hours. The contribution of the seasonal cycle component of the forecast was then subtracted from the measured surface currents. The standard deviation of the measurements less the seasonal cycle was 12.2 cm s^{-1}, shrinking the search radius down to 2.64 km after six hours. Next the 6-h forecasts of the seasonal anomalies created by the bilinear regressions were subtracted from the measurements along with the seasonal cycle. The combined effect of knowing both the seasonal cycle and the seasonal anomalies was to decrease the standard deviation to 6.7 cm s^{-1} and thus lower the search radius to 1.45 km. Finally, subtracting the residual component in addition to the seasonal cycle and anomalies brought the standard deviation at that point down to 6.5 cm s^{-1}. This effect of all three forecast components was that of the complete forecast, which made the final search radius 1.40 km for the six hour time span considered.

Since the standard deviations were for the total velocity $\left(\sqrt{U^2 + V^2}\right)$, the contributions of both U and V components were by default included in this calculation. The largest effect, as might have been guessed from looking at Figure 33, was seen from the contribution by the wind-driven seasonal anomalies. The residual, 18 hours old at the 6-h forecasts, has largely faded at this location and thus contributes little to the understanding of the currents. Also, at this location the seasonal cycle plays less of a role but, looking again at Figure 33, this would not necessarily have been the case at another place on the map.

4 Conclusion

An empirical statistical model was derived that predicted the wind-forced response of the surface currents off Oregon. First, a two year time series of hourly surface current maps made by HFR and winds measured by NDBC stations were gathered off the coast of Oregon (Figure 1). Tidal frequencies were filtered out of the wind and surface current time-series so that just the wind-forced portion of the surface currents would be considered. The seasonal cycle was likewise removed from these low-pass filtered data prior to EOF analysis so that their variance would not be dominated by seasonality (Figures 6 & 7). The first EOF of both the surface currents and the wind stress had a correlation of 0.83 with negligible lag, demonstrating that the seasonal anomalies of the low-pass filtered surface currents were strongly related to the wind stress (Table 2).

The EOFs of both the surface currents and measured winds showed a distinct shift in their spatial patterns north and south of Cape Blanco, Oregon (Figures 13 & 16). The time-varying EOF amplitudes of the seasonal anomalies of the surface currents also had a distinct correlation with both the V and U components of the winds that varied with NDBC station location (Table 3). Together, these results demonstrated that localized forecasts of the winds which capture both the alongshore and cross-shore variability in mesoscale resolution would be needed to accurately predict the wind-forced response of the surface currents.

The NAM model provided predictions of the vector winds off the Oregon coast in 12 km mesoscale resolution (Figure 1). Two years worth of predictions made by the NAM model at 17 separate forecast hours (each day at 0000 UTC and every three hours out until 48 hours into the future) were analyzed using EOFs. The EOFs of the time-series from all the forecast hours were seen to exhibit the separation north and south of Cape Blanco observed in the EOFs of the measured winds (Figure 24). Seasonal anomalies of the low-pass filtered NAM winds were interpolated to the locations of the NDBC stations so that the forecast and measured wind time series could be correlated. The correlation between the seasonal anomalies of the low-pass filtered NAM forecasts and NDBC measurements averaged 0.62 in τ^x and 0.75 in τ^y over all 17 forecast hours (Figure 27). Knowing the NAM model forecasts were reasonably well correlated with measurements of the coastal winds supported the use of NAM forecasts in predicting the wind-forced response of the ocean surface currents. Also seeing the shift in the NAM model winds occur (Figure 19) around the same time as the spring transition in the surface currents (Figure 7) supported the contention that variability forecast by the NAM model would be reflected in changes in the currents.

The low-pass filtered surface currents were considered to have three predictable terms: the wind-forced seasonal anomalies, the seasonal cycle, and a residual difference between measured and predicted surface currents:

For vector surface currents $\vec{u}$ at point $\vec{x}_i = (x_i, y_i)$ with i the gridpoint number and time t_n with n as the forecast hour

$$\vec{u}(\vec{x}_i, t_n) = \vec{u}_{\text{wind anomaly}}(\vec{x}_i, t_n) + \vec{u}_{\text{seasonal}}(\vec{x}_i, t_n) + \vec{u}_{\text{residual}}(\vec{x}_i, t_n).$$

Two year long time series of the seasonal anomalies of the low-pass filtered winds from each NAM forecast hour were linearly interpolated to the 6 km grid locations of the surface current measurements. A bilinear regression of the U and V components between these interpolated NAM winds and the seasonal anomalies of low-pass filtered surface currents was calculated for the time-series at each gridpoint so that $\vec{u}_{\text{wind anomaly}}(\vec{x}_i, t_n) = \vec{\alpha}_n(\vec{x}_i) \cdot \tau^x_{\text{NAM}}(\vec{x}_i, t_n) + \vec{\beta}_n(\vec{x}_i) \cdot \tau^y_{\text{NAM}}(\vec{x}_i, t_n) + \vec{\gamma}_n(\vec{x}_i)$. Adding these wind-forced seasonal anomalies of the surface currents to the seasonal cycle, $\vec{u}_{\text{seasonal}}(\vec{x}_i, t_n)$, yielded a prediction of the low-pass filtered surface currents. These low-pass filtered surface currents were then subtracted from the most recent detided measurements of surface currents from the HFR systems to yield a residual difference $\vec{u}_{\text{residual}}(\vec{x}_i, t_n)$. This residual was then added to each of the day's surface current forecasts in order account for the part of the current that was not predicted by local forecast wind, such as eddies or forecast errors.

$\vec{u}(\vec{x}_i, t_n)$ was predicted for 117 days between March 2, 2005 and July 10, 2005 to encompass all available data not included in the model setup. These low-pass filtered predictions of the surface currents were compared to low-pass filtered measurements of the surface currents made at the times of the forecasts. The results of this comparison showed that the skill of $\vec{u}(\vec{x}_i, t_n)$ was dependent on $\vec{x}_i$ (Figures 32A-32F) but correlations within the red regions were generally greater than 0.9 in the first forecast hour and decayed to values greater than about 0.7 out two days into the future. Correlations between the three individual forecast components and the measurements showed each of them to be dependent on location as well (Figures 32G-32X & Figure 33). The residual was most persistent in the region of the alongshore current jet (Figure 7 & Figures 32S-32X). The seasonal cycle likewise showed skill in its V component in the region of the coastal jet. The U component of the seasonal cycle most closely matched the surface currents in the lee of Cape Blanco (Figures 32P-32R & Figures 33J-33L). The wind-driven seasonal anomalies were correlated with measurements in excess of 0.6 throughout most of the grid in both U and V (Figures 32G-32L). The notable dips in correlation for the U component of $\vec{u}_{\text{wind anomaly}}(\vec{x}_i, t_n)$ were the regions alongshore and in the lee of Cape Blanco (Figures 32J-32L). In V, the poorest performance of $\vec{u}_{\text{wind anomaly}}(\vec{x}_i, t_n)$ was restricted to a single region in the southeast corner of the domain (Figures 32G-32I & Figures 33A-33C) where the predicted signal had instead largely been captured by the seasonal cycle (Figures 33G-33L).

The average difference between the V and U components of $\vec{u}(\vec{x}_i, t_n)$, the complete predictions of the V and U low-pass filtered surface currents, and the V and U low-pass filtered surface current measurements ranged from a high around 4 cm s^{-1} down through less than 0.5 cm s^{-1} (Figures 34A-34F). The error in the predictions grew as the forecasts got farther into the future, but the largest errors in both components, U and V, typically remained near 4 cm s^{-1} out through the two-day forecast.

4.1 Future Work

The obvious next-step to increase the utility of this model would be to include the tides. The time-series of surface currents measured by HFR include the tidal components. The now three-year record length in these surface current forecasts should be sufficient to extract the tidal components throughout the HFR grid.

Time series from moored current meters in the region of the HFR grid could also permit estimation of the baroclinic tide. Given the variability observed in the measurements of surface currents, particular challenges in predicting the baroclinic tidal components would be in determining the horizontal scales over which the available baroclinic time-series were coherent and forecasting these tides in a high enough resolution to complement the 6 km surface currents throughout the HFR grid domain.

This project only considered forcing by predicted winds above the prediction location. Previous studies have documented significant correlations between the sea level off the west coast and wind stress measured to the south (Halliwell & Allen, 1987). This signal has been attributed to coastally trapped waves. To account for this remote influence, correlations of the surface currents with winds farther south should be investigated.

The nature of the empirical statistical model presented in this paper is such that it can be used operationally, taking the forecasts from the NAM model at 0000 UTC and within minutes returning a complete set of predictions in three-hour time-steps out through two days into the future. O'Donnell et al. (2005) have already explored the use of HFR surface current measurements in search and rescue applications with very promising results. They extrapolated Eulerian velocity estimates 24 hours into the future using a combination of harmonic analysis for the tides and Gauss-Markov estimation for the non-tidal motion in Block Island Sound on the southern New England shelf (O'Donnell et al., 2005). The Gauss-Markov estimation used by O'Donnell et al. (2005) gave them predictions which differed from their HFR measurements by approximately 13 cm s^{-1} for the V component of the currents and 18 cm s^{-1} for the U component. The analysis presented in this paper predicted the non-tidal motion for regions off the Oregon coast out to 48 hours into the future, with predictions generally differing from HFR measurements by less than 4 cm s^{-1} in both U and V. The NAM model is now issuing forecasts out to 84 hours into the future. With a sufficient record of these extended forecasts, runs of the empirical statistical model presented in this thesis could be extended out to 3.5 days into the future.

When and if satellite (e.g., scatterometer) measurements are able to close the land-gap to overlap the HFR measurement grid, the empirical statistical model evolved in this paper could be formed between time-series of satellite winds and the surface current measurements made by HFR. Such an investigation would permit a direct comparison of measured wind forcing with the response of the surface currents over a scale and with a resolution not yet achieved.

Bibliography

Allen, J.S., Upwelling and coastal jets in a continuously stratified ocean, *Journal of Physical Oceanography*, *3* (3), 245-257, 4258446, 1973.

Barrick, D.E., M.W. Evans, and B.L. Weber, Ocean surface currents mapped by radar, *Science, 198*, 138-144, 1977.

Barrick, D.E. and B.J. Lipa, Evolution of Bearing Determination in HF Current Mapping Radars *Oceanography, 10*, 72-75, 1997.

Barrick, D.E. and B.J. Lipa, Radar angle determination with MUSIC direction finding. *United States Patent, No. 5,990,834*, 1999.

Barrick, D.E., Geometrical Dilution of Statistical Accuracy (GDOSA) in Multi-Static HF Radar Networks, *CODAR Ocean Sensors*, 2002, Available online at: *http://codaros.com/Manuals/Informative/GDOSA_Definition.pdf.*

Barth, J.A., S.D. Pierce, and R.L. Smith, A separating coastal upwelling jet at Cape Blanco, Oregon and its connection to the California Current System, *Deep-Sea Research (Part II)*, *47* (5-6), 783-810, 10.1016/S0967-0645(99)00127-7, 2000.

Beardsley, R.C., R. Limeburner, and L.K. Rosenfeld, Introduction to the CODE-2 moored array and large-scale data report. In *CODE-2: Moored Array and Large-Scale Data Report*, R. Limeburner, ed. Woods Hole Oceanographic Institution Technical Report, WHOI-85-35, 234 pp., 1985.

Black, T. L., The new NMC mesoscale Eta Model: Description and forecast examples. *Wea. Forecasting, 9***,** 265–278, 1994.

Blanton, B.O., OPNML/Matlab Routines, *Ocean Processes Numerical Modeling Laboratory*, Department of Marine Sciences, University of North Carolina at Chapel Hill, 2005, Available online at: *http://www.opnml.unc.edu/OPNML_Matlab/index.html*.

Chapman, R.D. and H.C. Graber, Validation of HF Radar Measurements. *Oceanography, 10*, 76-79, 1997.

Cook, M.S., and J.D. Paduan, Processing HF Radar Data using the HFRadarmap Software System, in *Radiowave Oceanography: The First International Workshop*, edited by J.D. Paduan, pp. 12-16, University of Miami, Timberline, Oregon 2001.

Cook, M.S., *HFRadarmap toolbox for MATLAB*, 2004, Available online at: *http://www.oc.nps.navy.mil/~radlab/HFRadarmapToolbox/.*

Davis, R.E., Predictability of Sea Surface Temperature and Sea Level Pressure Anomalies over the North Pacific Ocean, *Journal of Physical Oceanography*, *6* (3), 249-266, 1976.

Davis, R.E., Techniques for statistical analysis and prediction of geophysical fluid systems, *J. Geophys. Astrophys. Fluid Dyn*., *8*, 245-277, 1977.

Environmental Modeling Center, National Centers for Environmental Prediction, National Weather Service, National Oceanic and Atmospheric Administration, U.S. Department of Commerce, 2005, *National Centers for Environmental Prediction*, Available online at: *http://wwwt.emc.ncep.noaa.gov/.*

Gallus, W.A., The Impact of Step Orography on Flow in the Eta Model: Two Contrasting Examples, *Weather and Forecasting, 15*, 630-639, 2000.

Gordon, B.A., The WMO Format for the Storage of Weather Product Information and the Exchange of Weather Product Messages in Gridded Binary Form as Used by NCEP Central Operations, *Office Note 388, National Centers for Environmental Prediction*, 2002, Available online at: *http://www.nco.ncep.noaa.gov/pmb/docs/on388/.*

Halliwell, G.R, and J.S. Allen, Wavenumber-frequency domain properties of the coastal sea level response to alongshore wind stress along the west coast of North America, 1980-84, *J. Geophys. Res., 92 (11)*, 11761-11788, 1987.

Huyer, A., R.D. Pillsbury, and R.L. Smith, Seasonal variation of the alongshore velocity field over the continental shelf off Oregon, *Limnology and Oceanography*, *20*, 90- 95, 1975.

Huyer, A., E.J.C. Sobey, and R.L. Smith, The spring transition in currents over the Oregon continental shelf, *J. Geophys. Res.*, *84* (C11), 6995-7011, 1979.

Janjić, Z. I., The step-mountain eta coordinate model: Further developments of the convection, viscous sublayer, and turbulence closure schemes. *Mon. Wea. Rev., 122***,** 927–945, 1994.

Jones, B.H., and D. Halpern, Biological and physical aspects of a coastal upwelling event observed during March-April 1974 off northwest Africa, *Deep-Sea Res.*, *28* (1A), 71-81, 1981.

Kosro, P. M., Enhanced southward flow over the Oregon shelf in 2002: A conduit for subarctic water, *Geophys. Res. Lett. 30 (15)*, 8023, 2003.

Kosro, P. M., On the spatial structure of coastal circulation off Newport, Oregon, during spring and summer 2001 in a region of varying shelf width, *J. Geophys. Res., 110*, C10S06, doi:10.1029/2004JC002769, 2005.

Large, W.G., and S. Pond, Open Ocean Momentum Flux Measurements in Moderate to Strong Winds, *Journal of Physical Oceanography*, *11* (3), 324-336, 0144028, 1981.

Lipa, B.J., and D.E. Barrick, Least-squares methods for the extraction of surface currents from CODAR crossed-loop data: Application at ARSLOE, *IEEE J. of Oceanic Engineering*, *OE-8*, 226-253, 1983.

MathWorks, princomp :: Functions (Statistics Toolbox), 2005, Available online at *http://www.mathworks.com/access/helpdesk/help/toolbox/stats/princomp.html*.

National Data Buoy Center, National Weather Service, National Oceanic and Atmospheric Administration, U.S. Dept. of Commerce, 2005, *National Data Buoy Center*, Available online at: *http://www.ndbc.noaa.gov/.*

National Data Buoy Center, National Weather Service, National Oceanic and Atmospheric Administration, U.S. Dept. of Commerce, 2005, *National Data Buoy Center*, Available online at: *http://www.ndbc.noaa.gov/.*

O'Donnell, J., D. Ullman, C.A. Edwards, T. Fake, and A. Allen, The Operational Prediction of Circulation and Lagrangian Trajectories in the Coastal Ocean, Submitted to: *Atmospheric and Oceanic Technology*, July 27, 2005.

Perlin, N., R. M. Samelson, and D. B. Chelton, Scatterometer and model wind and wind stress in the Oregon - northern California coastal zone, *Monthly Weather Review, 132*, 2110-2129, 2004.

Rogers, E., T. Black, B. Ferrier, Y. Lin, D. Parrish, and G. DiMego, Changes to the NCEP Meso Eta Analysis and Forecast System: Increase in resolution, new cloud microphysics, modified precipitation assimilation, modified 3DVAR analysis. *NWS Technical Procedures Bulletin 488*, NOAA/NWS, 2001.

Schmidt, R.O., Multiple emitter location and signal parameter estimation, *IEEE Trans. Antennas Propag., vol. AP-34, no.3*, 276–280, 1986.

Sciremammano, F., A Suggestion for the Presentation of Correlations and Their Significance Levels, *Journal of Physical Oceanography, 9*, 1273-1276, 1979.

Strub, P.T., J.S. Allen, A. Huyer, and R.L. Smith, Large-scale structure of the spring transition in the coastal ocean off western North America, *Journal of Geophysical Research*, *92* (C2), 1527-1544, 1987a.

Strub, P. T., J. S. Allen, A. Huyer, R. L. Smith, and R. C. Beardsley, Seasonal cycles of currents, temperatures, winds, and sea level over the Northeast Pacific continental shelf: 35 degree N to 48 degree N, *J. Geophys. Res.*, *92(C2)*, 1507–1527, 1987b.

Trenberth K.E., W.G. Large, and J.G. Olson, 1990, The mean annual cycle in global ocean wind stress, *Journal of Physical Oceanography* 20 (11): 1742–1760.

University Corporation for Atmospheric Research, Cooperative Program for Operational Meteorology, Education and Training, 1998, *Eta Model Characteristics: Background Information*, Available online at: *http://www.comet.ucar.edu/nwplessons/etalesson2/characteristicsbackground.htm*.

University Corporation for Atmospheric Research, Cooperative Program for Operational Meteorology, Education and Training, 2002, *Top Ten Common Numerical Weather Prediction (NWP) Misconceptions: The Analysis Should Match Observations*, Available online at: *http://meted.ucar.edu/norlat/tencom*.

Xue, M., K.K. Droegemeier, V. Wong, A. Shapiro and K. Brewster, ARPS Version 4.0 User's Guide, 380pp, Available from *CAPS, University of Oklahoma*, Norman OK 73019, USA, 1995.

APPENDICES

Appendix A Screening HFR Radial Velocities

HFR sites transmit a radio wave signal and, using the principle of Bragg scattering, the returning sea-echo is processed to obtain the bearing of the ocean waves that caused the scattering, the distance to the waves, and the speed of the waves toward or away from the site (Barrick et al., 1977; see Section 1.1). From these data, maps of ocean surface currents are produced. This process of determining wave speed, direction, and distance is subject to interference from other radio-wave sources, objects in the vicinity of the antennas, and reflection of the instrument's own signal off the ionosphere.

In an effort to remove spurious surface velocity measurements from data taken by standard and Long-Range CODAR SeaSondes, a program was written in MATLAB to identify these suspect values in files produced by the HFRadarmap toolbox for MATLAB (Cook & Paduan, 2001; Cook 2004). Titled HFR2DiffScreen (a truncation of "High Frequency Radio 2nd Difference Screener"), the program calculates a given percentile of the "second-differences" between these radial velocity measurements, in both space and time, and flags as "bad" the data that fall outside the user-defined acceptable range. With the parameters specified by the user, HFR2DiffScreen automates the process of screening HFR surface current measurements. This screening helped to minimize instances of "bad" measurements entering into the calculation of total surface currents, invalidating the surface currents at those HFR gridpoints where the "bad" readings were incorporated.

HFR2DiffScreen calculates the “second-difference” in space (S_{2nd}) by computing the difference between the radial velocity at each point (i, j) and the average of the radial velocities at up to eight surrounding points [(i±1,j±1), (i±1,j±1)], less any missing points. The “second-difference” in time (T_{2nd}) is calculated from the difference between each measurement and the mean of the radial velocities at that point from up to two hours before and two hours after, less any missing hours.

The user-specified percentiles of S_{2nd} and T_{2nd} are then calculated and any gridpoints whose values fall outside either of the given percentiles are flagged as “bad.” This removes those measurements from consideration that are the most different from their neighbors, differences frequently attributable to direction finding errors and ionospheric reflection. Additionally, any measurement for which either S_{2nd} or T_{2nd} could not be calculated due to a lack of measurements is deemed “bad”, as these isolated points are often found over land due to errors in direction finding or toward the edge of the measurement field of the long-range HFR sites from ionospheric reflections.

As an additional precaution against including radial velocity measurements misplaced over land, an angle-limit file can be used that acts as a land mask to ensure that all measurements are over water. The user also has the option of specifying upper limits for both S_{2nd} and T_{2nd} (ulS_{2nd} and ulT_{2nd}) so that any measurement whose “second difference” in cm s^{-1} exceeds the given limit is marked as “bad.”

Finally, the user has the option of specifying three percentages: the percentage of the time-series for which there must be radial velocity measurements at each location ($Rvel_{\%}$), the percentage of S_{2nd} values each point must have ($S_{\%2nd}$), and the percentage of T_{2nd} values each point must have ($T_{\%2nd}$). In this way, points with insufficient data records ($Rvel_{\%}$), or those that made sporadically ($T_{\%2nd}$) or in sparsely sampled regions ($S_{\%2nd}$) can be excluded.

The values for these parameters used in screening the long-range (6 km grid) SeaSonde measurements were:

99^{th}: percentile for both S_{2nd} and T_{2nd}
angle-limits: land-mask
ulS_{2nd}: 20 cm s^{-1}
ulT_{2nd}: 30 cm s^{-1}
$Rvel_{\%}$, $S_{\%2nd}$, and $T_{\%2nd}$: 10%

These values resulted in an approximately 15% reduction in the radial velocity time series from each HFR site. Of that 15%, approximately 2% of those values were over water with the remaining 13% being direction-finding errors over land. The use of the GDOP baseline mask (see Section 2.1) removed from consideration those areas where the majority of the 2% of “bad” measurements over water were found to occur. Within the regions specified in Figure 11, the data reduction attributable to HFR2DiffScreen was 1% or less.

Appendix B Prediction of Seasonal Anomalies of Low-pass Filtered Surface Currents using EOFs

An alternate method of calculating $\vec{u}_{\text{wind anomaly}}(\vec{x}_i, t_n)$ (see Section 3.4) was derived that made use of the EOFs calculated in Section 3.2. As demonstrated previously in Table 2, there was a distinct correlation between the first EOF of the seasonal anomalies of the surface currents and the seasonal anomalies of the wind stress as measured by the NDBC stations. This correlation between the surface currents and the winds held true for the EOFs calculated from the seasonal anomalies of the NAM model forecasts (Table B1).

Table B1. Lagged correlations between the first two surface current seasonal anomaly EOF amplitude time-series and the EOF amplitude time series from the seasonal anomalies of the first predictive NAM forecast hour, 3-h forecast. Higher EOFs were found to be uncorrelated. Correlations for HFR EOF 1 vs. NAM EOF 1 and HFR EOF 2 vs. NAM EOF 2 were elevated over all forecast hours. Lags are given in hours with positive lag meaning that the series indicated by the row is best correlated with an earlier point in the series specified by the column. Statistically insignificant (95% confidence) correlations are in parentheses.

	0300 UTC NAM			
	EOF 1		EOF 2	
	corr.	lag	corr.	lag
Surface Currents				
EOF 1	0.84	0	(-0.19)	48
EOF 2	(-0.20)	72	0.47	0

Given the agreement between EOF 1 vs. EOF 1 and EOF 2 vs. EOF 2 of the surface current measurements and NAM forecasts, a regression was formed between these EOFs to relate the time-varying amplitudes of their modes (Figure B1; Table B2).

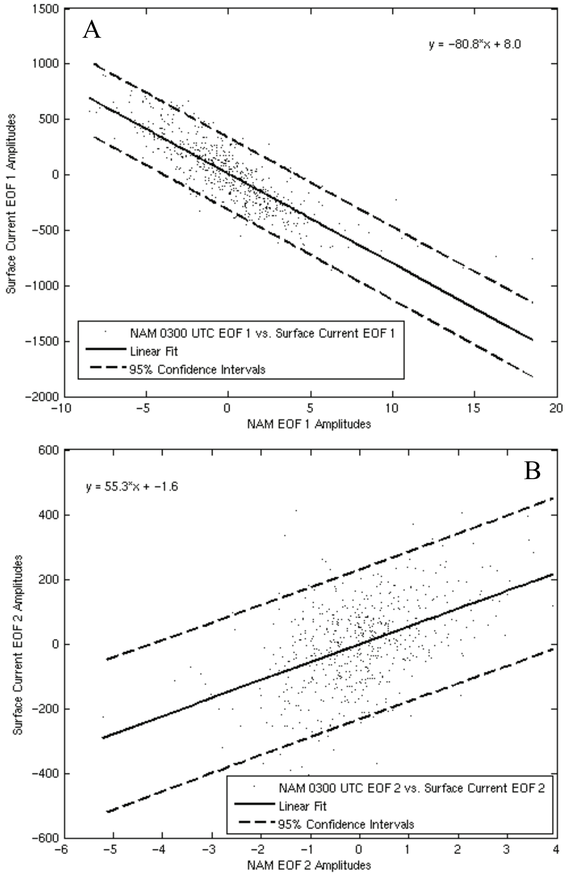

Figure B1. EOF amplitudes from the seasonal anomalies of the low-pass filtered NAM 3-h forecast wind stresses vs. EOF amplitudes from the seasonal anomalies of the low-pass filtered surface current measurements. Panel A is for EOF 1 vs. EOF 1. Panel B is for EOF 2 vs. EOF 2. Linear regression is the solid line with equation. 95% confidence intervals are the dashed lines.

Table B2. Slope and intercept of the linear regression between the time-varying amplitudes (S) of EOFs 1 and 2 of the NAM forecast hours and EOFs 1 and 2, respectively, of the surface currents measured by HFR.

$$S_{HFR} = \alpha + \beta S_{NAM}$$

	EOF 1 Currents vs. EOF 1 NAM		EOF 2 Currents vs. EOF 2 NAM	
Forecast Hour	slope (β)	intercept (α)	slope (β)	intercept (α)
0-h	-87.1	7.8	58.3	-1.2
3-h	-80.8	8.0	55.3	-1.6
6-h	-81.5	7.9	51.8	-2.1
9-h	-83.1	6.1	51.5	-0.1
12-h	-84.9	9.0	53.4	-1.1
15-h	-87.1	7.6	54.9	-1.1
18-h	-89.7	8.8	57.8	-0.1
21-h	-87.4	5.5	51.5	0.6
24-h	-82.3	7.9	44.7	0.7
27-h	-79.7	8.1	48.0	0.3
30-h	-80.4	7.8	54.2	-0.1
33-h	-79.7	7.3	49.4	1.5
36-h	-78.3	8.5	47.9	0.9
39-h	-81.3	7.0	49.6	1.2
42-h	-83.8	7.2	42.5	0.9
45-h	-82.1	4.1	33.9	2.2
48-h	-79.0	6.4	31.8	1.4

There was a noticeable drop in the slope of the regressions between the NAM and surface current EOF amplitude time-series in the later forecast hours, particularly in the second EOF. This was expected since the NAM wind forecasts were known to become less accurate for times farther into the future (Figure 27). Nonetheless, the regressions, even at the later forecast hours, were considered sufficient for prediction given their significant correlation with the surface currents and what was still a substantial linear slope.

The crux of the ability to transform an incoming NAM wind forecast into a prediction of the surface currents was the conversion of the forecast into a series of amplitudes using the previously calculated EOFs (Section 3.2). The U and V components of the 10 m wind speed from all the day's forecast hours were collected from the subset of locations within the NAM grid shown in Figure 1. These wind speeds were then converted to seasonal anomalies of the low-pass filtered wind stress, τ^x and τ^y, as before in Section 3.1. These steps mirrored the processing that went into the creation of the EOFs calculated from the collected NAM forecasts over the analyzed two years.

This prepared the present NAM forecasts for the real work of being transformed into predictions of the seasonal anomalies of the low-pass filtered surface currents. This was done by converting the NAM predictions into EOF amplitudes and, using the regressions given in Table B2, then transforming the NAM EOF amplitudes into surface current EOF amplitudes. Defining D_{NAM} as the concatenated τ^x and τ^y data from the input NAM forecast hour, S_{NAM} as the time-varying amplitudes of the NAM EOFs (or, as they are more eloquently known outside of oceanographic circles, scores), C_{NAM} as the EOF mode shapes (also known as coefficients), and D_{HFR}, S_{HFR} and C_{HFR} the equivalent of these for the surface currents measured by HFR, the following derivation demonstrates how the NAM forecasts could be converted into EOF amplitudes and how these amplitudes could then be made into values for the surface currents:

$$\begin{aligned}
&\mathrm{D_{NAM}} = \mathrm{C_{NAM}} \cdot \mathrm{S_{NAM}^T} \\
&\mathrm{C_{NAM}^T} \cdot \mathrm{D_{NAM}} = \mathrm{C_{NAM}^T}\left(\mathrm{C_{NAM}} \cdot \mathrm{S_{NAM}^T}\right) \\
&\mathrm{S_{NAM}^T} = \mathrm{C_{NAM}^T} \cdot \mathrm{D_{NAM}} \\
&\mathbf{S_{NAM}} = \left(\mathbf{C_{NAM}^T} \cdot \mathbf{D_{NAM}}\right)^{\mathbf{T}}
\end{aligned}$$

using the line above allowed the NAM data to be transformed directly into EOF amplitudes; these amplitudes from just the first two NAM EOFs could then be converted into surface current EOF amplitudes via the regressions (Table B2)…

$$\text{take } \mathrm{S}_{\mathrm{NAM}}(\mathrm{EOF}\,1\,\&\,2) \xrightarrow{\text{regression}} \mathrm{S}_{\mathrm{HFR}}(\mathrm{EOF}\,1\,\&\,2)$$

$$\mathbf{C}_{\mathbf{HFR}} \cdot \mathbf{S}_{\mathbf{HFR}}^{\mathbf{T}} = \mathbf{D}_{\mathbf{HFR}}$$

With the last line, the surface current EOF amplitudes derived via regression are transformed into surface current data.

The above method of using EOFs to convert NAM forecasts into surface currents produced results comparable to those achieved via the bilinear regressions (Figure 31). The predictions via EOFs worked well because there was a significant correlation between the first and second NAM and surface current EOFs (Table B1). The EOF analysis presented in Section 3.3 comparing both the NBDC measurements and NAM forecasts of the winds to the surface current measurements showed that the first EOF captured primarily the V component in each time-series. The second EOF of the surface currents was largely the U component of the flow and correlations showed that EOF 2 of the surface currents was forced by both the V and U components of the wind (Table 3). Thus, as was stated in Section 2.4.2, it was necessary to utilize a predictive scheme that took into account the U and V components of the wind in the prediction of both the V and of the U surface currents. Since these were vector EOFs, calculated from a concatenation of both the U and V components of the currents and of the winds, this predictive scheme satisfied that requirement.